JOURNAL OF AIRCRAFT
Vol. 46, No. 2, March–April 2009

Standard Unstructured Grid Solutions for Cranked Arrow Wing Aerodynamics Project International F-16XL

Stefan Görtz*
Royal Institute of Technology (KTH), 100 44 Stockholm, Sweden
A. Jirásek†
Swedish Defence Research Agency (FOI), 164 90 Stockholm, Sweden
Scott. A. Morton‡
U.S. Air Force SEEK EAGLE Office, Eglin AFB, Florida 32542
David R. McDaniel§ and Russell M. Cummings¶
U.S. Air Force Academy, USAF Academy, Colorado 80840
and
John E. Lamar** and Khaled S. Abdol-Hamid††
NASA Langley Research Center, Hampton, Virginia 23681-2199

DOI: 10.2514/1.35163

Steady and unsteady viscous flow simulations of a full-scale, semispan, and full-span model of the F-16XL-1 aircraft are performed with three different computational fluid dynamics codes using a common unstructured grid. Six different flight conditions are considered. They represent Reynolds and Mach number combinations at subsonic speeds, with and without sideslip. The steady computations of the flow at these flight conditions are made with several Reynolds-averaged Navier–Stokes turbulence models of different complexity. Detached-eddy simulation, delayed detached-eddy simulation, and an algebraic hybrid Reynolds-averaged Navier–Stokes/large-eddy simulation model are used to quantify unsteady effects at the same flight conditions. The computed results are compared with flight-test data in the form of surface pressures, skin friction, and boundary-layer velocity profiles. The focus of the comparison is on turbulence modeling effects and effects of unsteadiness. The overall agreement with flight data is good, with no clear trend as to which physical modeling approach is superior for this class of flow. The Reynolds-averaged Navier–Stokes turbulence models perform well in predicting the flow in an average sense. However, some of the flow conditions involve locally unsteady flow over the aircraft, which are held responsible for the scatter between the different turbulence modeling approaches. The detached-eddy simulations are able to quantify the unsteady effects, although they are not consistently better than the Reynolds-averaged Navier–Stokes turbulence models in predicting the flow in an average sense in these flow regions. Detached-eddy simulation fails to predict boundary-layer profiles consistently over a range of flow regimes, with delayed detached-eddy simulation and hybrid Reynolds-averaged Navier–Stokes/large-eddy simulation models offering a remedy to recover some of the predictive capabilities of the underlying Reynolds-averaged Navier–Stokes turbulence model. Nonetheless, the confidence in the predictive capabilities of the computational fluid dynamics codes with regard to complex vortical flowfields around high-performance aircraft of this planform increased significantly during this study.

Nomenclature

a	=	speed of sound
b	=	wing span
C_p	=	pressure coefficient $= (p - p_\infty)/q_\infty$
c	=	mean aerodynamic chord $= 7.53$ m (24.7 in.)
c_f	=	local skin friction coefficient $= \tau/q_\infty$
h	=	aircraft altitude
k	=	turbulent kinetic energy
M	=	Mach number $= U/a$
p	=	pressure
$p_{\text{stat/tot}}$	=	static/total pressure
q_∞	=	dynamic pressure $= \rho_\infty U_\infty^2/2$
Re	=	Reynolds number $= \rho_\infty U_\infty c/\mu_\infty$
r	=	radial distance
$T_{\text{stat/tot}}$	=	static/total temperature
t	=	time
U	=	velocity
V/V_{RE}	=	ratio of velocity magnitude in boundary layer to that at the rake extreme total-pressure tube
x, y, z	=	x axis positive aft, y axis to the right, z axis vertically upward or normal to surface at a rake location
y^+	=	dimensional wall distance, used to judge the initial cell spacing normal to boundary layer surfaces
α	=	angle of attack
β	=	angle of sideslip
Δt	=	time-step size
Δ_0	=	average cell size in the focus region
ε	=	turbulent dissipation rate
μ	=	viscosity coefficient
ρ	=	density

Received 16 October 2007; revision received 11 July 2008; accepted for publication 15 July 2008.

*Research Scientist; Present Affiliation: German Aerospace Center (DLR), Lilienthalplatz 7, 38108 Braunschweig, Germany. Member AIAA.
†National Research Council Research Associate; Present Affiliation: U.S. Air Force Academy, USAF Academy, CO 80840. Member AIAA.
‡Senior Research Scientist, 205 West D. Avenue, Suite 346. Associate Fellow AIAA.
§Research Engineer, Department of Aeronautics, 2410 Faculty Drive Suite 108. Member AIAA.
¶Professor of Aeronautics, Department of Aeronautics, 2410 Faculty Drive Suite 108. Associate Fellow AIAA.
**NASA Langley Distinguished Research Associate. Associate Fellow AIAA.
††Senior Research Scientist, Configuration Aerodynamics Branch, Mail Stop 499. Associate Fellow AIAA.

τ = shear stress
ω = specific turbulent dissipation rate
∞ = freestream values

I. Introduction

THE basic data of [1], as highlighted and detailed in [2], provide the background for this article, which focuses on those computational fluid dynamics (CFD) contributions to the Cranked Arrow Wing Aerodynamics Project International (CAWAPI) from research organizations that employed a common unstructured grid (referred to as "standard" unstructured grid hereafter) with their flow solvers. In particular, this paper summarizes the contributions made by the Royal Institute of Technology (KTH), the Swedish Defence Research Agency (FOI), the U.S. Air Force Academy (USAFA), and NASA Langley Research Center (NASA). KTH and FOI joined forces to concentrate on turbulence modeling aspects, whereas the USAFA focused on determining the unsteady characteristics of the flowfield using detached-eddy simulation (DES), including a time-step study. NASA Langley Research Center examined the ability of its two-equation linear and nonlinear k–ε turbulence models to represent the flow physics around the F-16XL. Detailed results from the aforementioned participants are drawn from [3–5]. The contributions of other CAWAPI participants are summarized in [6,7].

This paper begins with a description of the flight conditions to be computed for comparison by CAWAPI members. Next is a description and comparison of the flow solvers that participants used to contribute solutions to CAWAPI. The results of the time-step study conducted by the USAFA are presented. This is followed by a brief presentation of the specifics of the standard unstructured grid, which is described in more detail in [8,9]. The computed results are discussed and compared to flight-test data in the main section of the paper.

II. Flight Conditions

Seven of the 99 CAWAP flight conditions (FC) [1] were selected for computation in CAWAPI. They represent different Reynolds and Mach number combinations at subsonic and transonic speeds, with and without sideslip. All seven flight conditions are listed with their nominal and actual values in Table 1.

Flight conditions 7, 19, and 46 are medium angle-of-attack vortical flow conditions at various subsonic Mach numbers and altitudes, whereas FC70 is a low angle-of-attack attached flow condition at a transonic Mach number of 0.97. Note that results for FC70 are not presented here, but can be found in [3–5]. Flight conditions 50 and 51 are also medium angle-of attack vortical flow conditions, but at sideslip angles of +5.31 and −4.58 deg, respectively, and a mirrored full-span grid created from the standard grid was used. Flight condition 25 is at a high incidence angle and most interesting in terms of unsteady modeling.

All seven flight conditions were computed by the three organizations contributing to this paper, but with different physical and numerical modeling, as described next and as summarized in Table 2. Note that all calculations were made assuming fully turbulent flow. Flight conditions 7, 19, 25, 46, and 70 have zero nominal sideslip and were computed by all three codes as symmetric using the semispan standard unstructured grid, although the actual sideslip angles ranged from +0.725 to −0.133 deg. For the full-span model simulations at FC50 and FC51, the actual angle of sideslip was specified. The angle of attack was set to the actual angle of attack for all flight conditions.

III. Computational Methods

A. Edge (KTH/FOI)

KTH and FOI joined forces and used Edge [10] for contributing to CAWAPI. Edge is a flow solver for unstructured hybrid grids of arbitrary elements. The code is a proprietary code of FOI where it is being developed. The code is shared with other users, among them KTH, based on a license agreement. User development of Edge is

Table 1 Subset of CAWAP flight conditions (FC) chosen for CAWAPI

	Nominal					Actual			
FC	M_∞	α, deg	β, deg	Re/ft	h, ft	M_∞	α, deg	β, deg	Re
FC7	0.29	13.0	0.0	1.79×10^6	5,000	0.304	11.89	−0.133	44.40×10^6
FC19	0.32	13.0	0.0	1.71×10^6	10,000	0.360	11.85	+0.612	46.80×10^6
FC25	0.24	20.0	0.0	1.28×10^6	10,000	0.242	19.84	+0.725	32.22×10^6
FC46	0.51	10.0	0.0	1.77×10^6	24,000	0.527	10.40	+0.684	46.90×10^6
FC50	0.42	13.0	+5.0	1.46×10^6	24,000	0.434	13.56	+5.310	39.41×10^6
FC51	0.42	13.0	−5.0	1.46×10^6	24,000	0.441	12.89	−4.580	38.96×10^6
FC70	0.98	3.6	0.0	3.6×10^6	22,300	0.970	4.37	+0.310	88.77×10^6

Table 2 Contributions by organization

Contributor	Turbulence models used	Numerics	FC conditions	Steady/ unsteady	Ref.
USAFA	SARC, SARC-DES, SARC-DDES	CC, Godunov type with least-square reconstruction, implicit with Newton method	FC7, FC19, FC25, FC46, FC50, FC51, FC70	S,U	AIAA 2007-0493
KTH/FOI	Spalart–Allmaras, EARSM k–ω, w/ and w/o rotational correction, Hellsten k–ω w/ and w/o rotational correction; DRSM; DES, hybrid RANS-LES	NC, central, explicit Runge–Kutta, dual time stepping	FC7, FC19, FC25, FC46, FC50, FC51, FC70	S,U	AIAA 2007-0678
NASA	Spalart–Allmaras, two-equation linear k–ε, nonlinear ARSM k–ε	CC, Roe finite difference scheme, Roe finite volume scheme, AUSM, Harten, Lax, and van Leer with contact discontinuity; implicit, dual time stepping, Newton method	FC7, FC19, FC25, FC46, FC50, FC51, FC70	S	AIAA 2007-0682

shared with FOI. The flow solver, which was written to run on parallel computers, uses an edge-based formulation and a node-centered (NC), finite-volume scheme to solve the compressible Reynolds-averaged Navier–Stokes (RANS) equations. For steady flows, the equations are integrated toward steady state with an explicit multistage Runge–Kutta scheme. To accelerate convergence, implicit residual smoothing and a multigrid technique can be employed. Low Mach number preconditioning is also available. The spatial discretization is either second order central or second order upwind.

Time-accurate calculations are done either by Runge–Kutta time marching with a global time step or by implicit time marching with explicit subiterations, so-called "dual time stepping" [11].

An adaptive mesh refinement module allows for local h refinement of the hybrid grid by cell subdivision based on a sensor that measures a gradient in the solution. In addition, there are three sensors for identifying vortices. They are based on the total-pressure ratio, the production of entropy, and an eigenvalue analysis of the velocity gradient tensor.

The Edge code contains several eddy-viscosity turbulence models based on the Boussinesq hypothesis as well as a suite of explicit algebraic Reynolds-stress models (EARSM). Their implementation in Edge follows that of Wallin and Johansson [12]. The EARSM model has been used in combination with two types of k–ω models—the standard k–ω model [13] and the Hellsten k–ω model [14]. For flows with streamline curvature, curvature-corrected versions of these models are also available [15]. Edge also contains the differential Reynolds-stress model (DRSM) described by Hanjalic et al. [16], an algebraic hybrid RANS-LES (large-eddy simulation) model [17,18] and DES [19] capability.

Concerning CAWAPI, the steady flow solutions were computed using the second-order accurate central scheme for the mean flow equations and a second-order upwind discretization of the turbulence equations. The Courant–Friedrichs–Lewy (CFL) number was set to 1.0. Convergence acceleration was achieved through local time stepping, residual smoothing, and full multigrid with three levels. Fully turbulent flow was assumed and the solutions were initialized with freestream conditions which were computed from the flight conditions in Table 1 assuming the atmospheric properties of the 1976 Standard Atmosphere. All flight conditions were computed with the Spalart–Allmaras turbulence model, k–ω EARSM with and without rotational correction, and the Hellsten k–ω EARSM with and without rotational correction. Note that the curvature-corrected versions of the k–ω EARSM have been considered here because the uncorrected models tend to overestimate the eddy viscosity in vortical flow. Rotational correction limits the maximum eddy viscosity in the vortex core. In addition, FC19 and FC46 were computed with the DRSM. Time-accurate computations were performed for FC7, FC25, and FC46 using both the standard DES and the algebraic hybrid RANS-LES models. The time step was chosen according to the guidelines for DES by Spalart [20] and the results of a time-step study conducted by the USAFA, which is summarized below. The inner-loop CFL number was set to 1.0 and a fixed number of 50 inner iterations was specified. The time-dependent flow simulations were initialized with the steady-state solution computed with the Spalart–Allmaras turbulence model. The transient part of the solution was not considered when computing the average solution. For FC7 the unsteady flow solution was averaged over 3000 physical time steps. FC25 was averaged over 12,000 time steps.

Table 3 Propulsion conditions as a function of the flight condition (FC)

	Engine inflow conditions				Engine outflow conditions	
FC	T_{stat}, K	p_{stat}, Pa	U, m/s	M	T_{tot}, K	p_{tot}, Pa
FC7	276.7	75,842	115.7	0.347	583.3	158,579
FC19	269.9	70,327	105.4	0.320	583.3	148,237
FC46	246.4	40,334	123.2	0.390	580.6	102,042
FC70	288.3	73,429	141.6	0.416	666.7	206,843

The boundary conditions were symmetry, adiabatic wall for the surface of the aircraft, and characteristic variable freestream conditions for the far-field boundaries, which were located about 10 aircraft length (24 root chord lengths) away from the aircraft. The boundary conditions on the engine inlet face and the exhaust mixing plane were pressure outlet and total states inlet, respectively. The corresponding propulsion conditions are listed for the different flight conditions in Table 3. It should be noted that these conditions are generic engine conditions and do not correspond to any specific engine.

B. Cobalt (USAFA)

The U.S. Air Force Academy used the commercial flow solver Cobalt [21]. Cobalt is a cell-centered, finite-volume CFD code. It solves the unsteady, three-dimensional, compressible RANS equations on hybrid unstructured grids. Its foundation is based on

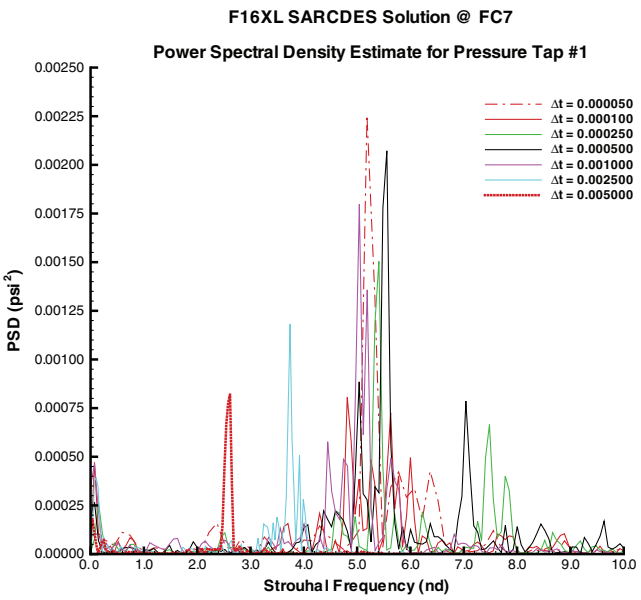

a)

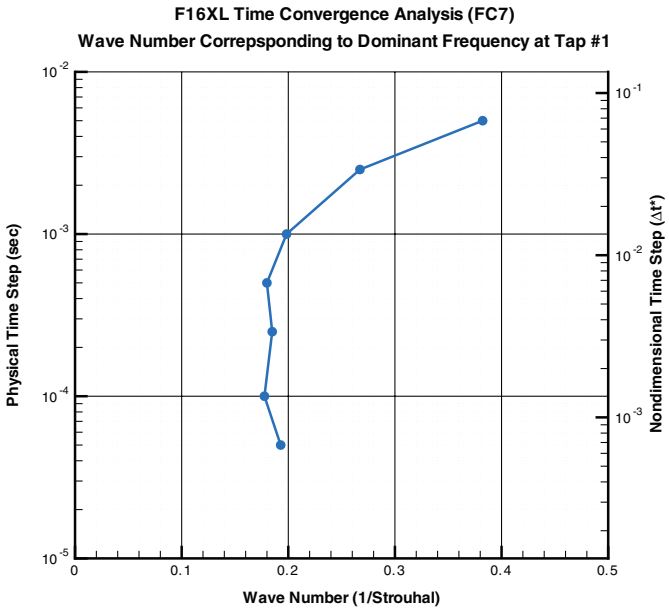

b)

Fig. 1 Time-step study at FC7: power spectral density results a) and wave number variation with time step b) for pressure tap 1.

Godunov's first-order accurate, exact Riemann solver. Second-order spatial accuracy is obtained through a least-squares reconstruction. A Newton subiteration method is used in the solution of the system of equations to improve time accuracy of the point-implicit method.

Strang et al. [21] validated the numerical method on a number of problems, including the Spalart–Allmaras model [22], which forms the core for the DES model available in Cobalt. Tomaro et al. [23] converted the code from explicit to implicit, enabling CFL numbers as high as 10^6. Grismer et al. [24] parallelized the code, with a demonstrated linear speedup on as many as 4000 processors. The parallel METIS (ParMETIS) domain decomposition library of Karypis et al. [25] is also incorporated into Cobalt. New capabilities include rigid-body and 6 degrees of freedom (DOF) motion, equilibrium air physics, and delayed DES (DDES) [26].

With respect to CAWAPI, steady flow solutions and initiation of time-accurate solutions were computed using the RANS turbulence model of Spalart–Allmaras with rotation corrections (SARC), first order accuracy in time, and a time step commensurate with a CFL number of 1 million. Time-accurate solutions were computed with the DES and DDES hybrid RANS-LES turbulence models with SARC as the underlying RANS model. A time-step study was conducted to determine the proper time step for the flight condition and grid combination used for this study and is the subject of the next section. Nominally, each solution (corresponding to a flight condition from Table 1) was initialized by completing 3000 flow solution iterations with second-order spatial accuracy, first-order time accuracy with the time-step size determined by the global minimum CFL number, and 1 N subiteration per time step. From these initial solutions, at least 6000 additional iterations were performed with a specified time-step size and second-order spatial and temporal accuracy with 3 N subiterations. Typically, the last 2000 iterations of each run were time averaged to compute the average solution values in the results, and time-accurate flow solution files were exported every five time steps during this time period. Unsteady bounds could be determined by interrogating these flow solution files.

The boundary conditions were symmetry, adiabatic solid wall for the surface of the aircraft and the engine duct, and modified Riemann invariants for the far-field boundaries. A source boundary condition based on Riemann invariants was used to create an inflow condition at the engine exhaust. A sink boundary condition was used at the engine face to model the corrected engine mass flow.

C. USM3D (NASA)

NASA researchers used USM3D, the flow solver portion of the NASA Tetrahedal Unstructured Software System (TetrUSS) [27]. USM3D uses a cell-centered, finite volume to solve the compressible RANS equations on unstructured all-tetrahedral grids. For steady flows, the equations are integrated toward steady state with an implicit point Gauss–Seidel or explicit Runge–Kutta scheme. Newton time stepping or dual time stepping can be used for time-dependent flow calculations. Several upwind schemes are implemented into USM3D, among them Roe's flux-difference splitting, the advection upstream splitting method (AUSM) scheme, van Leer flux vector splitting, and the Harten, Lax, and van Leer scheme with contact restoration.

The version of USM3D used for CAWAPI features a range of turbulence models including the Spalart–Allmaras one-equation model, Menter's shear-stress transport model, and a suite of two-equation linear and nonlinear (algebraic Reynolds-stress model) k–ε models. A DES capability based on the Spalart–Allmaras model is also available.

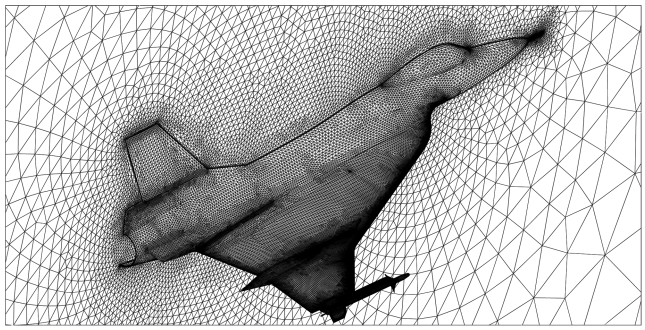

Fig. 2 F-16XL-1 standard unstructured grid on the aircraft surface and in the symmetry plane.

Special features include static aero/structural coupling, solid and deforming grid motion, overset Chimera grids, feature-based grid adaptation, and 6-DOF motion.

For CAWAPI, USM3D was used to compute steady flow solutions with Roe's flux-difference splitting scheme. Convergence to steady state was accelerated using the point-implicit Gauss–Seidel scheme. FC46 was computed with the Spalart–Allmaras turbulence model and the two-equation linear and nonlinear k–ε models. All remaining flight conditions were modeled with the two-equation linear k–ε model.

The boundary conditions were symmetry and adiabatic wall for the surface of the aircraft. The engine was modeled in the code by using the specific boundary condition types, that is, engine intake or exhaust, and the associated values of temperature, pressure (or a ratio of that to the freestream value), along with a Mach number at the inlet and exhaust/mixing plane for each FC (see Table 3).

D. Code Comparison

USM3D and Cobalt are based on a cell-centered (CC) discretization, whereas Edge is a vertex- or node-based code. The implications of this seemingly subtle difference have to be understood and considered when comparing results computed with the two approaches on a common grid. The difference stems from the fact that a tetrahedral grid of N vertices contains from $5N$ to $6N$ cells. Thus, a cell-centered approach on a tetrahedral mesh will contain many more degrees of freedom than a vertex-centered discretization on the same mesh, and can therefore be expected to yield higher accuracy and require higher computational expense [28]. In other words, an advantage for the cell-centered approach is its ability to achieve acceptable accuracy on relatively coarse grids. However, the vertex-based discretization can be expected to be more accurate than a cell-based discretization using an equivalent numbers of unknowns, because the former approach will result in a larger number of flux calculations. Although numerical experiments conducted by Mavripilis [29] and others have verified the superior accuracy of cell-centered approaches versus vertex-based approaches on identical grids, but also suggested the vertex-based approach to be the most efficient approach overall, the issue has never been decided conclusively, in large part due to the lack of fully consistent comparisons between the two approaches using identical discretizations and solvers.

Note that this issue is most important for tetrahedral meshes and is of only secondary importance on hexahedral grids. For prismatic element meshes, such as those often used in boundary-layer regions, the differences between cell-centered and vertex-based approaches are less pronounced than for tetrahedral meshes, but still significant [28].

Table 4 Summary of family of standard unstructured grids

Grid	Tetrahedra	Prisms	Pyramids	Nodes	Surface elements	Prism layers	Used by
Tetrahedral	14,802,429	0	0	2,534,132	160,266	0	NASA
Hybrid	10,485,709	1,442,394	0	2,535,842	160,266	9	KTH/FOI, USAFA
Mod. hybrid	7,716,197	2,285,124	120,661	2,535,842	160,266	<20	KTH/FOI

E. Physical Time-Step Study

The accurate prediction of unsteady flow about the F-16XL required both a good grid and an appropriate physical time step and the USAFA therefore conducted a time-step study. The choice of the physical time step depends on the time scales of the flow features of interest and may thus not be known a priori. A grid of a particular fineness coupled with a specific time step which is adequate for a computation required to resolve vortical flow features will be inadequate for resolving smaller turbulent structures. In the latter case, a finer grid and a smaller time step will be necessary. If the time step is too large, the simulation may fail to capture important flow features and mimic unphysical steady behavior. Taking detailed flow "measurements" within the flowfield region of interest is the only way to properly determine an appropriate time step. Therefore, a series of "pressure taps" was located in a region of the flowfield where a primary leading-edge vortex intersected with the air-dam vortex which will be described in Sect. V.

Figure 1a shows the variation of power spectral density of the pressure time history at pressure tap 1 for seven time steps, ranging from $\Delta t = 5.0 \times 10^{-3}$ to 5.0×10^{-5} s. These time steps were chosen based on the rule of thumb that aerodynamic features of interest are usually resolved at nondimensional time steps of approximately $\Delta t^* = \Delta t \cdot U_\infty / c = 0.01$. As can be seen, as the time step is decreased, the primary frequencies begin to coincide at a common frequency, which we consider time-step "convergence." The results for pressure tap 1 are consolidated and shown as a function of the time step and the wave number of the dominant mode in Fig. 1b. The figure strongly suggests that the primary wave number is converging to a constant value as the time step decreases, with a wave number of approximately 0.19 reached when the physical time step is below $\Delta t = 10^{-3}$ s. Although a converged time step has been attained at $\Delta t = 10^{-3}$ s, a smaller time step may be desirable for accurate flow prediction. It is also clear that the Strouhal frequency for the primary flow feature is in the neighborhood of 5, which corresponds to a helical mode instability.

Although an additional time study could be performed to determine the effect of the number of Newton subiterations on the solution, experience [30] shows that 3 N subiterations are usually sufficient for accurate prediction of unsteady flows about full-scale aircraft with Cobalt. Based on the time-step study all unsteady calculations with Cobalt and Edge were performed with a physical time step of $\Delta t = 5.0 \times 10^{-4}$ s, corresponding to $\Delta t^* = 0.0066$. The result of the time-step study is in good agreement with the guidelines for DES by Spalart [20], which suggest a physical (outer) time step of $\Delta t = \Delta_0 / U_{\max} \approx 2.5 \times 10^{-4}$ s, where the average cell size Δ_0 in the focus region was estimated to equal 0.05 m for the grid used here and the maximum velocity $U_{\max}$ in the LES (or focus) region equal to twice the freestream velocity.

IV. Standard Unstructured Grid and Hybrid Grid Generation

Although some attempts have been made to define an "equivalent" grid for comparing cell-based and vertex-based codes at equivalent accuracy levels, for example, in the recent Drag Prediction Workshop series [31], this approach has not been adopted here. This is partly due to the fact that this approach for defining equivalent resolutions for cell-based and vertex-based grids has only been studied for transonic flows and may not apply equally for other types of flows, particularly for cases where off-body flow physics, that is, vortical flows, are of primary importance [28], as is the case here.

The standard unstructured grid for use with all three flow solvers was generated by NASA. It is described in detail in [8,9]. For the sake of completeness it must be pointed out that the grid generation approach followed by NASA is unconventional in that thin layers of right-angled tetrahedral cells are generated in the boundary-layer region by the advancing-layers method (ALM). Unlike the conventional advancing-front method (AFM), which introduces cells in the field in a totally unstructured manner, the ALM generates layers of thin tetrahedral cells in a more orderly fashion while maintaining many advantageous features of the AFM. Outside the boundary layer a regular, nearly isotropic (inviscid) tetrahedral grid is generated by the AFM. The transition from thin layers to the regular grid is gradual and continuous because a common background grid is used to control both methods.

The final all-tetrahedral grid for calculation of the viscous flow over the half-span, full-scale model of the F-16XL-1 is made up of 2,534,132 nodes, corresponding to 14,802,429 cells, and an average value of y^+ of less than 1. The maximum y^+ value of about 2 occurs underneath the primary wing vortex. This grid was used by NASA with USM3D. A 3-D view of the surface grid and symmetry plane is shown in Fig. 2.

Note that for numerical reasons Edge and Cobalt require the use of hybrid grids, where cell shapes that do not become skewed with stretching (e.g., hexahedra and prisms) are used in the viscous flow regions and tetrahedral cells away from viscous regions. To fulfill that requirement, the all-tetrahedral grid was converted into a hybrid grid by combining the first nine layers of high-aspect-ratio, semistructured tetrahedral cells off the aircraft surface into layers of prismatic cells. This operation reduced the cell count to a total of

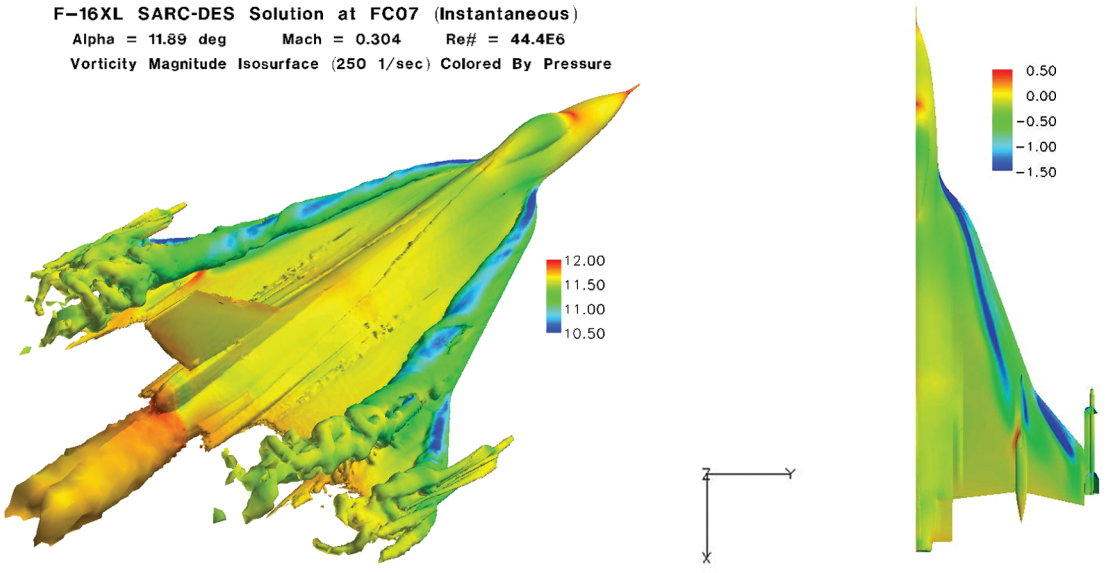

a) b)

Fig. 3 Flight condition 7: a) isosurfaces of vorticity magnitude colored by pressure; b) surface pressure coefficient distribution, C_p.

11,928,103, corresponding to 2,535,842 nodes. It is important to note that the transition between the admittedly relatively few prismatic layers and the tetrahedral grid is very smooth, because there are several semistructured ALM-generated viscous layers on top of the prismatic layers. The hybrid grid was used by the USAFA and KTH/FOI with Cobalt and Edge, respectively.

To investigate the influence of the number of prismatic layers on the accuracy of the results computed with the codes that require hybrid grids, a third standard unstructured grid with up to 20 prismatic layers was generated from the all-tetrahedral grid. This grid featured "chopped" prismatic layers with pyramids as end caps. It was used by KTH with Edge. The statistics of the entire family of standard grids are summarized in Table 4. For flight conditions with nonzero sideslip the half-span grids were mirrored at the symmetry plane.

V. Results and Discussion

The CFD solutions obtained with the three different flow solvers for the different flight conditions are compared to flight data in the form of measured surface pressures, boundary-layer profiles, and local skin friction. This is followed by a discussion of the discrepancies between the solutions obtained with the different

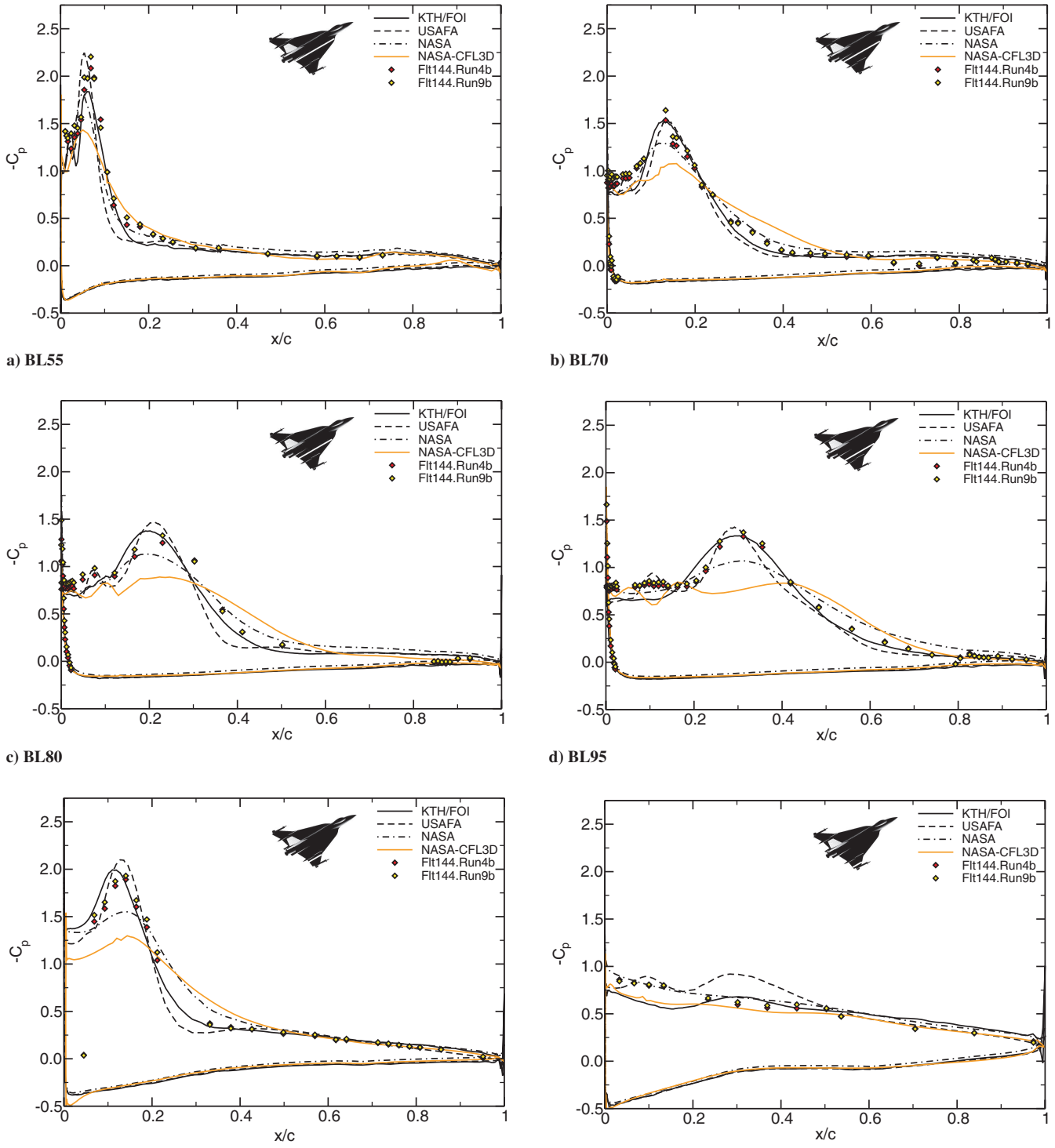

a) BL55 b) BL70

c) BL80 d) BL95

e) BL153.5 f) BL184.5

Fig. 4 Surface pressure coefficient for FC7 at various butt line stations, compared to flight-test data ($M_\infty = 0.304$, $\alpha = 11.89$ deg, and $Re = 44.40 \times 10^6$).

solvers. Finally, some possible reasons for the differences between the computed results and the flight data are given.

For the sake of clarity, only selected computational results are compared to the measured data. The full set of results is reported by each participating organization in [3–5]. The results from KTH/FOI were obtained with the Hellsten k–ω EARSM model without rotational correction, unless otherwise noted in the legend or accompanying text, and those from NASA with the linear k–ε model. The USAFA results are time averaged SARC-DES data, unless noted otherwise. In the different cross plots, the KTH/FOI results are represented by solid black lines, those from NASA by dot-dashed black lines or black circle symbols, and those from the USAFA by black dashed lines, unless otherwise noted in the legend. The flight measurements are represented by black diamond symbols with different fill colors.

To demonstrate progress compared to previous computational investigations of the F-16XL-1, the present wall-resolved numerical results are also compared to data from Lamar et al. [1] and Lamar [32], who performed a flight, wind-tunnel, and CFD comparison for subsonic and transonic speeds using the structured flow solver CFL3D. The CFL3D solver used the Baldwin–Lomax turbulence model with the Degani–Schiff modification [33] (in the $j-k$

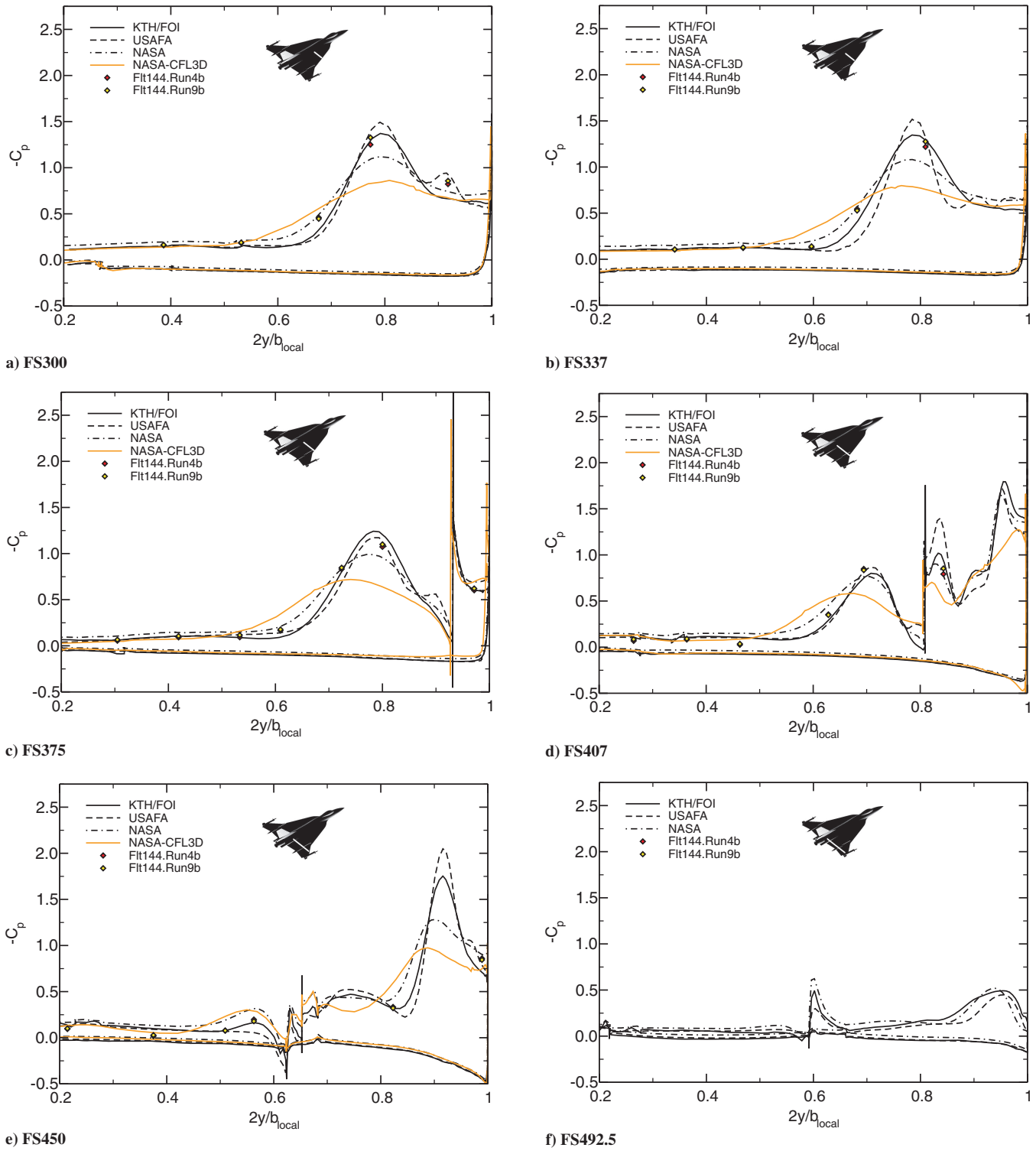

Fig. 5 Surface pressure coefficient for FC7 at various fuselage stations, compared to flight-test data ($M_\infty = 0.304$, $\alpha = 11.89$ deg, and $Re = 44.40 \times 10^6$).

directions) on a relatively coarse multiblock, patched grid (1,372,096 cells) and wall functions because the first cell height y^+ value was 82. The CFL3D results are represented by solid orange lines in the cross plots, where applicable.

In the subsequent sections, data will be presented with the nomenclature of butt line (BL) and fuselage stations (FS). The coordinate system used for analyzing the flight and CFD data is orthogonal with x measured aft, y measured outboard on the starboard side, and z measured up, with an origin near the nose of the aircraft. A BL is an x–z plane at a constant y coordinate and the numerical designation gives the distance from the symmetry plane to the BL plane. An FS is a y–z plane at a constant x coordinate and the numerical designation gives the distance from the nose to the FS plane.

A. Results at Medium Angle-of-Attack Flight Conditions Without Sideslip (FC7, 19, 46)

There are four nominally symmetric flight conditions with angles of attack greater than 10 deg and subsonic Mach numbers. Three of the flight conditions are considered a medium angle of attack in the range of 10 to 12 deg (FC7, FC19, and FC46). The fourth condition, FC25, is considered a high angle-of-attack condition because it has an angle of attack nearly twice that of the other three flight conditions and is dedicated a separate section. This section presents results for the first three flight conditions.

1. *Flight Condition 7*

FC7 is at an angle of attack of 11.89 deg, a Mach number of 0.304, and an altitude of 5000 ft, resulting in a Reynolds number of 44.4×10^6 based on the mean aerodynamic chord. This condition was used by the CAWAPI Research and Technology Organization (RTO) Task Group as an initial comparison case for the various research teams. Unfortunately, this particular case had no flight-test data to use for comparison. The solutions for FC7 are therefore compared to flight-test data for FC49 (Flt144-run4b with $M_\infty = 0.42$, $Re = 36.06 \times 10^6$) and FC34 (Flt144-run9b with $M_\infty = 0.37$, $Re = 39.03 \times 10^6$), which is for the same nominal angle of attack and sideslip angle but a slightly different nominal Mach and Reynolds number.

Figure 3 depicts the flowfield over the F-16XL at FC7 computed with Cobalt. Isosurfaces of vorticity magnitude of 250 1/s colored by pressure are shown in the perspective view (Fig. 3a) and surface C_p for the right wing is shown in the planform view (Fig. 3b). It is apparent that the dominant features of the flowfield are the leading-edge vortex originating from the swept wing leading edge inboard of the crank, the air-dam vortex originating from the air dam protruding forward of the actuator pod at the wing upper surface, the outer-wing vortex originating from the wing leading edge outboard of the crank, and a complicated set of vortices from the air intercept missile (AIM)-9 fins and forebody. It can also be seen that the leading-edge vortex changes characteristic from a coherent structure to a complex structure with helical windings, similar to vortex breakdown, in the region of the actuator pod. It is also interesting to note that the helical vortex structure is above the vortex emanating from the air dam creating a very complex structure. In addition to these vortices, other vortical structures, such as the inner wing secondary vortex, are present. All flight conditions characterized by vortical flow exhibit a similar vortical flow structure, although the strength and location of the vortices may differ.

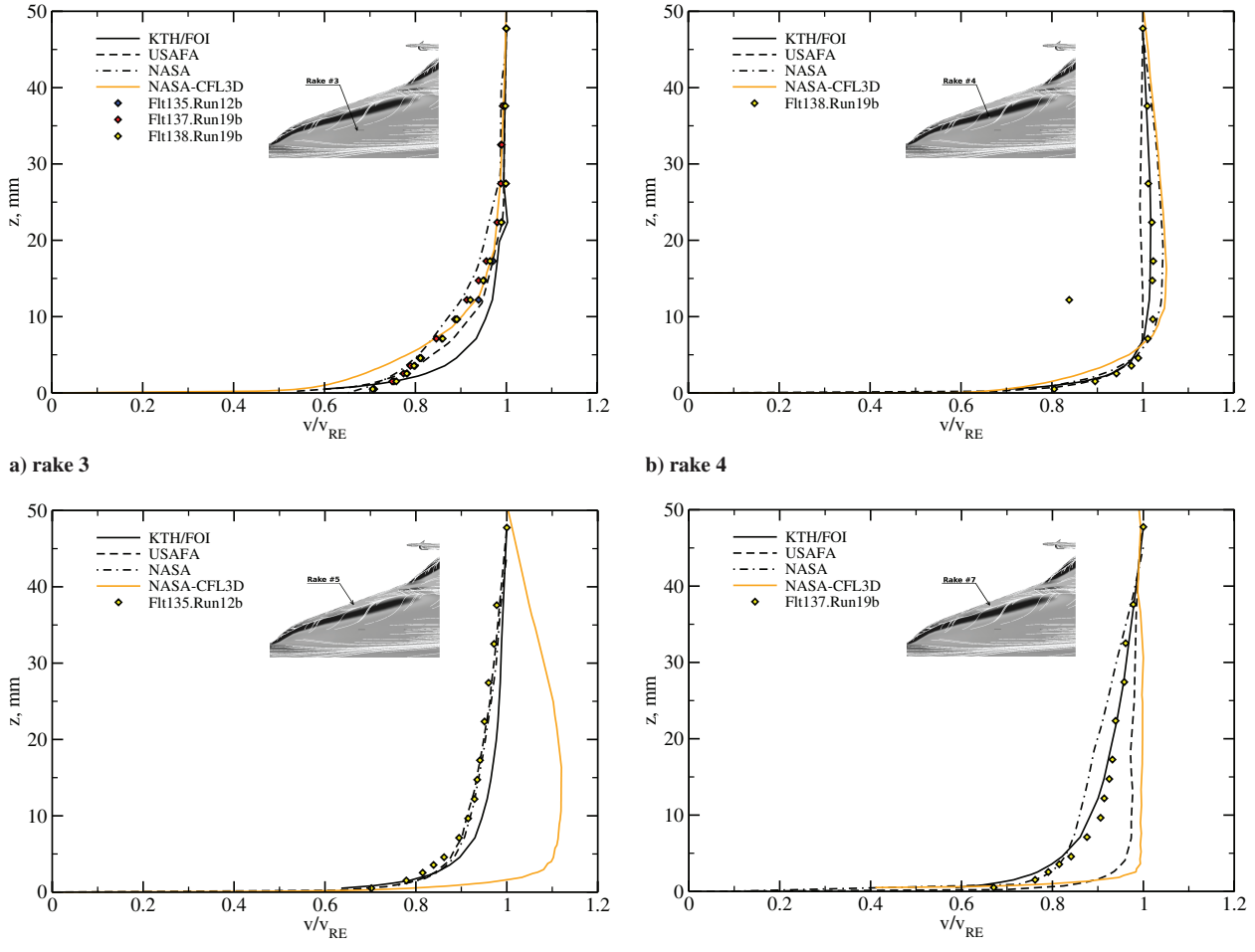

Fig. 6 Boundary-layer profiles computed with steady RANS turbulence models for FC7, compared to flight-test data ($M_\infty = 0.304$, $\alpha = 11.89$ deg, and $Re = 44.40 \times 10^6$).

The surface pressure distributions measured in flight for FC49 and FC34 are compared to the numerical results for FC7 in Figs. 4 and 5, which show the pressure coefficient C_p as a function of the nondimensional chordwise distance from the leading edge at a range of butt lines (BL) and fuselage stataions (FS), respectively. By and large, the most important characteristics of the surface pressure distribution, such as primary and secondary suction peaks underneath the primary and secondary vortices, are well predicted from a qualitative point of view in Fig. 4. However, the magnitudes of the primary and secondary suction peaks are generally underpredicted by the linear k–ε model employed by NASA (USM3D) and the recovery from the strong suction peak is too gradual for this model. This is true for all butt lines and fuselage stations. The time-averaged DES (USAFA) results show good agreement with the available flight-test data at BL55 through BL95 with only minor discrepancies near the recovery from the strong suction peak. The suction peak C_p value and the position of the peak are in good agreement for all of these BL locations. At BL153.5 the computed suction peak is somewhat higher than the experimental value. It is surprising that the DES model fails to predict the correct C_p distribution at BL184.5, which is in a region of presumed flow unsteadiness. The steady RANS results are remarkably accurate here; even the wall-functions model predicts the trend observed in the measurements. The Hellsten k–ω EARSM model (KTH/FOI) is best in predicting the recovery downstream of the primary suction peak at all butt lines, whereas it underpredicts the suction peak at BL55 and the secondary suction peak at BL70 through 95.

As is true of all BL positions, the distributions of surface pressure coefficients at all FS positions are in good overall agreement with the available flight-test data, with the exception of the NASA CFL3D and USM3D results and the USAFA DES results at FS337, where the pressure recovery is too steep inboard of the primary suction peak.

The results of a turbulence modeling study conducted by KTH/FOI [3] for this flight condition (not shown here) found only minor differences between the Hellsten k–ω EARSM model predictions for C_p and those of k–ω EARSM and Hellsten k–ω EARSM with rotational correction. However, the Spalart–Allmaras model failed to predict the pressure distribution both in terms of the chordwise location and magnitude of the primary suction peak as well as the width of the footprint of the primary vortex. All of the RANS models underpredicted the secondary suction peak.

The paper by the USAFA [4] demonstrated for this flight condition that at BL153.5, BL184.5, FS407.5, FS450, and FS492.5 there were large fluctuations in C_p, especially near the vortex induced suction peak. This unsteadiness was found to be due to the interaction of the vortices from the air dam/actuator pod, outer wing crank, and the AIM-9 tip missile and resulted in large variations in C_p in this region.

Next, the measured and computed boundary-layer profiles are compared. The boundary-layer measurements were made by using two rakes at a time at four different positions on the left wing with the most inboard one used as a control [1]. Each rake used 16 active tubes, 15 for total pressure and 1 for static pressure, of the 23 available. The overall height of the rakes was 2 in. (5.08 cm). When mounted on the airplane, each rake was oriented into the local flow at an average angle over its height based on initial CFD predictions from the NASA CFL3D code. These angles were measured from the centerline with the rake pointing forward and inboard and have values of 7.5, 45, 27.5, and 23.5 deg, for rakes nos. 3, 4, 7, and 5, respectively. The rakes were at a nominal position of FS295 at locations along a line approximately perpendicular to the leading

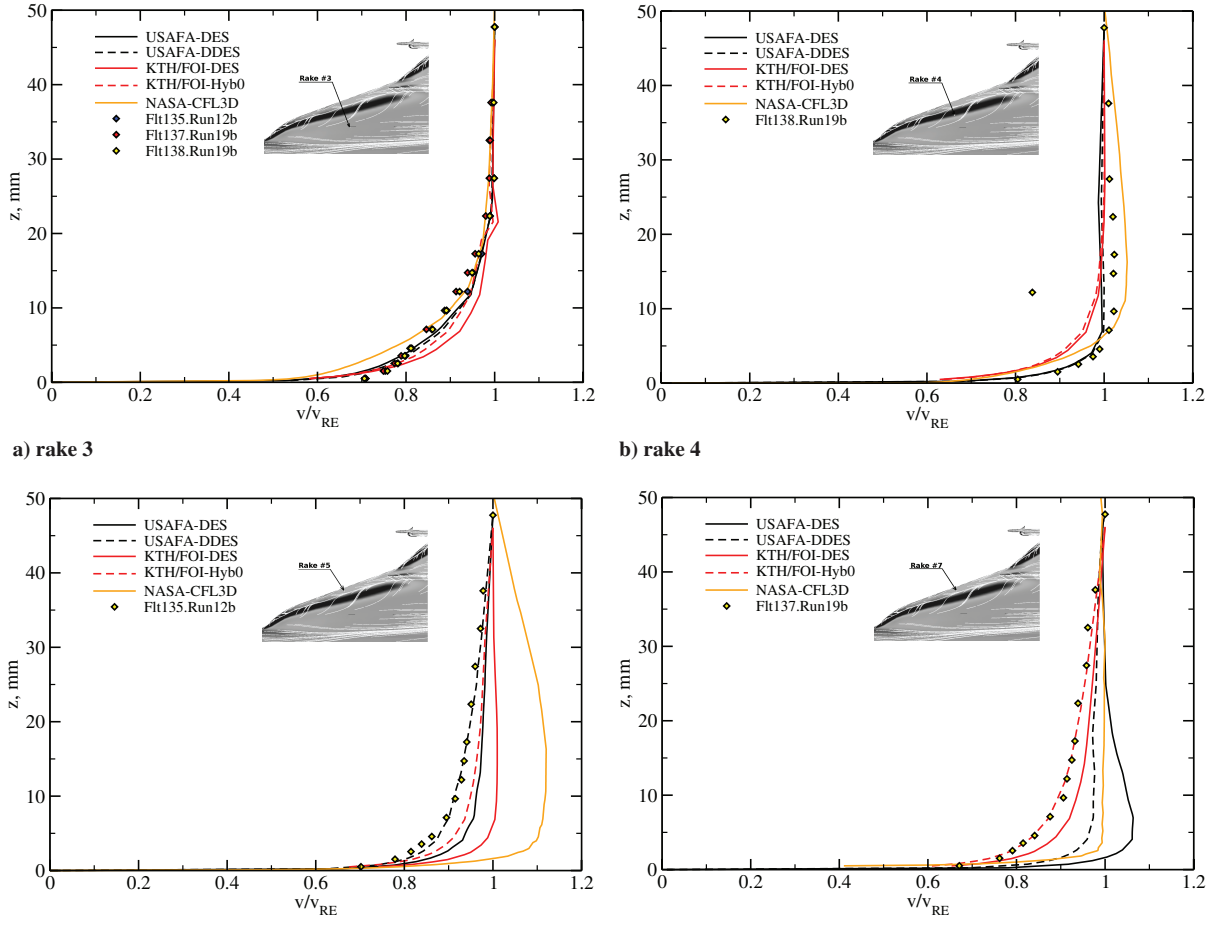

a) rake 3 b) rake 4

c) rake 5 d) rake 7

Fig. 7 Time-averaged boundary-layer profiles computed with different hybrid RANS-LES models for FC7, compared to flight-test data ($M_\infty = 0.304$, $\alpha = 11.89$ deg, and $Re = 44.40 \times 10^6$).

edge with rake 3 most inboard, rake 5 very near the leading edge, and rakes nos. 4 and 7 in between. The general arrangement of the rake positions can be seen in Fig. 8 of [2] and a photo of a rake mounted on the aircraft can be seen in Fig. 6 of that reference. The four locations were chosen as follows: one well inboard of the shed vortex systems where the flow is nearly streamwise (rake 3), one underneath the primary wing vortex (rake 4), one underneath the secondary vortex (rake 5), and one at the secondary separation line (rake 7).

The postprocessing needed to determine the boundary-layer profiles from the numerical solutions for comparison with the measured boundary-layer rake data was not straightforward, because the velocities needed to be established along a normal to the surface at the specified points in order to be comparable with the rake data. Nevertheless, the velocity profiles were extracted from the CFD solutions at exactly the locations where the flight-test data were measured using the rake probes. The first step of the extraction procedure included identifying a grid cell on the surface containing the coordinates of a probe BL/FS location. The grid nodes of this cell on the surface were then used to calculate the corresponding surface normal vector. Because the distribution of the total-pressure probes was known from the rake geometry, the physical coordinates were defined using the normal vector and rake geometry data. The velocity vectors were then interpolated from the surrounding mesh nodes. At each point, the magnitude of velocity as well as the three components of the velocity vector were computed. The velocity profile used for comparison with the experimental data was computed by projecting the velocity vector in the rake direction using the rake orientation angles given previously.

Figure 6 shows the comparison between the boundary-layer profiles measured at rake locations 3, 4, 7, and 5, respectively, and the unstructured grid steady-state RANS solutions by KTH/FOI and NASA. The comparison of the velocity profiles for rake 3, which is estimated to be inboard of the primary vortex position, shows very good agreement between the NASA results with the linear k–ε model and the measured data (Fig. 6a). The velocity profile predicted by KTH/FOI with the Hellsten k–ω EARSM model is in general disagreement with the measured values for $z < 20$ mm (0.8 in.). This comes somewhat as a surprise because rake 3 is located where the flow is streamwise and attached, which should be fairly easy to predict. Note that all four turbulence models employed by KTH/FOI for this flight condition predicted this boundary-layer behavior for rake 3 although only the results computed with the Hellsten k–ω EARSM model without rotational correction is shown (see Fig. 19 in [3] for the results computed with all four turbulence models). The velocity profile predicted by CLF3D using wall functions is rounder.

The comparison of the velocity profiles underneath the anticipated location of the primary vortex (rake 4) demonstrates excellent qualitative and quantitative agreement between the wall-resolved solutions and the measured data (Fig. 6b). Even the NASA CLF3D predictions with the wall-function model compare well with the flight data. Looking in more detail, it can be observed that both the measurements and the CFD solutions indicate a "jet-type" flow to commence for $z > 6$ mm (0.25 in.). Both also show regions of quasi-linear variation of the velocity with y, indicative of being outside the boundary layer and just in the influence of the primary vortex. Note, however, that the USM3D and CFL3D solutions exhibit a more jet-

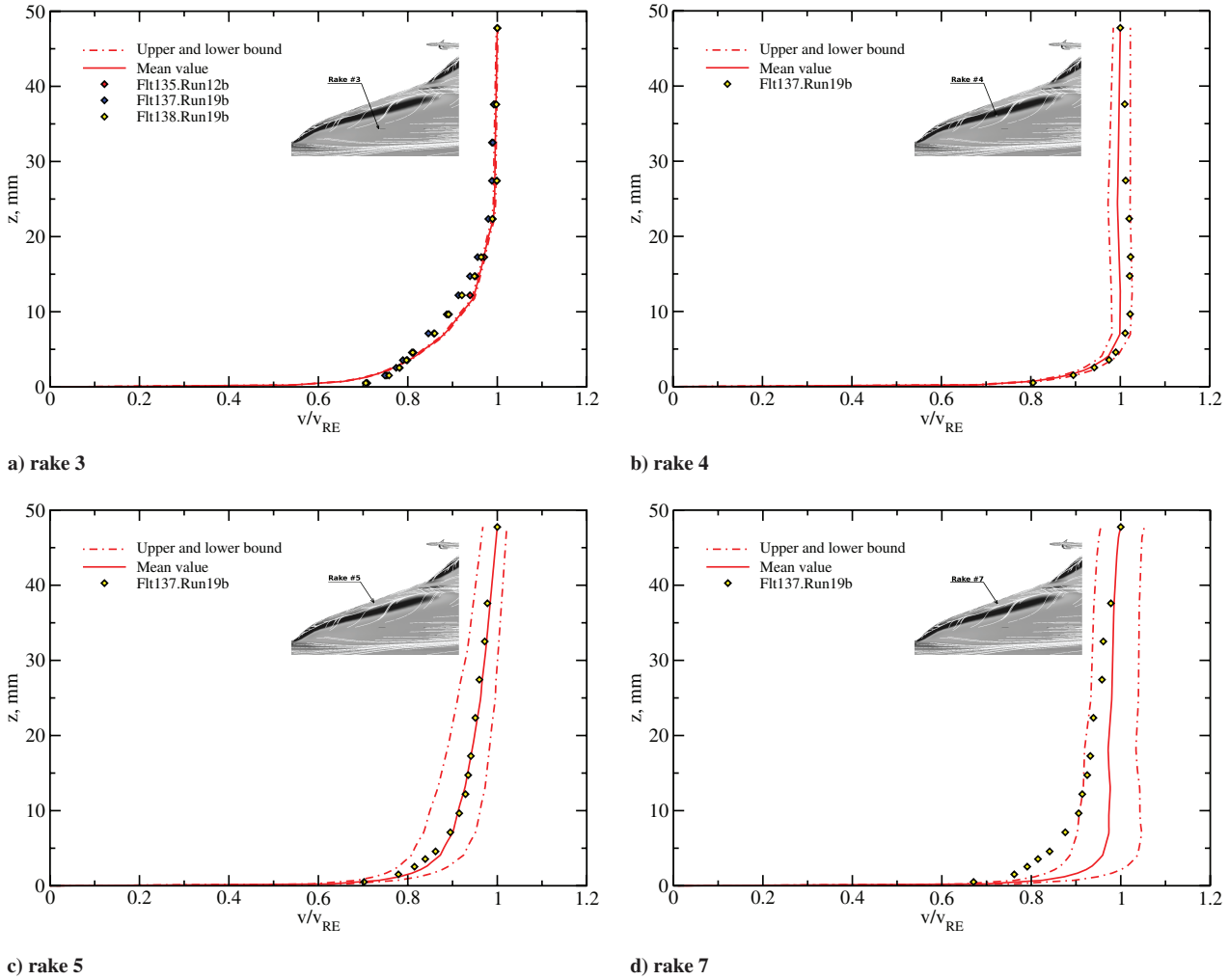

Fig. 8 Computed average boundary-layer profiles and unsteady bounds from DES for FC7, compared to flight-test data ($M_\infty = 0.304$, $\alpha = 11.89$ deg, and $Re = 44.40 \times 10^6$).

type behavior than the measured velocity profile, which is very well predicted by the Hellsten k–ω EARSM model in Edge (KTH/FOI). Note that KTH/FOI also computed a stronger jet-type flow at rake location 4 with the Spalart–Allmaras turbulence model in Edge (not shown here, see [3]).

Underneath the estimated location of the secondary vortex (rake 5), Fig. 6c, the measurements suggest a slightly retarded velocity profile, which is qualitatively and quantitatively predicted by NASA's linear k–ε model, whereas the numerical solution predicted by KTH/FOI with the k–ω EARSM model exhibits a somewhat "fuller" velocity profile. KTH/FOI computed a more retarded flow at rake location 5 with the Spalart–Allmaras model (not shown). The wall-functions model in CFL3D (NASA) predicted a jetlike velocity profile, presumably because the log-layer assumptions underlying this model are not valid here. Note that the measured profile for rake 5 achieves edge velocity beyond the rake extreme. The quasi-linear growth of velocity for $z > 13$ mm (0.5 in.) for this profile appears to be associated with vortices around these boundary-layer rakes because the velocity field produced outside an isolated vortex core varies as $1/r$.

The comparison at the presumed location of the secondary separation line (rake 7), shown in Fig. 6d, is very favorable for Edge (KTH/FOI), whereas NASA's USM3D code predicted a velocity profile which is more retarded between $z = 5$ mm (0.2 in.) and 40 mm (1.6 in.) when compared to the experimental data. The velocity profile predicted by NASA with the wall-function model (CFL3D) is completely inadequate at this rake location, with a linear velocity profile from the boundary-layer edge almost all the way to the wall. Note that apparently the measured velocity is not asymptotic to the boundary-layer edge velocity at the rake extreme; this leads to the conclusion that the maximum velocity has not been achieved at this location. Unfortunately, no clear trend as to which turbulence model/code is better in predicting all four velocity profiles can be observed other than that the wall-functions model is inappropriate for this type of flow. This demonstrates that none of the turbulence models is capable of modeling all of the different flow regimes well and indicates that the most suitable turbulence model varies from regime to regime.

In Fig. 7 the measured boundary-layer rake data are compared to time-averaged DES and DDES data computed with Cobalt by USAFA (black solid and dashed lines), and time-averaged DES and algebraic hybrid RANS-LES data computed with Edge by KTH/FOI (red solid and dashed lines). Both DDES and the hybrid modeling approach are techniques primarily aimed at the problems of standard DES modeling, which exhibits an incorrect behavior in, for example,

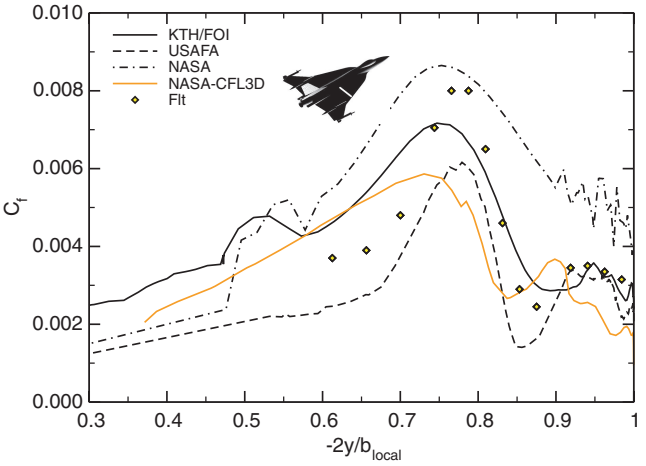

Fig. 9 Local skin friction coefficient for FC19 ($M_\infty = 0.36, \alpha = 11.85°$, $Re = 46.8 \times 10^6$).

thick boundary layers and shallow separation regions, where the LES region penetrates the boundary layer and gives rise to the wrong solution, depending on the local grid density [26]. This is the case, for example, for fine grids, where the switch from RANS to DES can take place somewhere inside the boundary layer and produce premature (grid-induced) separation [34,35].

Rake 3, which is well inboard of the primary leading-edge vortex, shows the best overall agreement between flight data and the numerical results (Fig. 7a). There is no difference between the USAFA DDES and DES solutions, while the hybrid model solution by KTH/FOI is closer to the experimental data than the velocity profile predicted with DES. Nonetheless the DES results from KTH/FOI are in better agreement with the flight-test data than those obtained with the Hellsten k–ω EARSM model shown in Fig. 6a. Note that the USAFA found essentially no unsteady effects for this rake location. This is evident from Fig. 8a, which shows computed average boundary-layer profiles (solid red lines) and unsteady bounds (red dot-dashed lines) from DES compared to flight-test data.

For rake 4, the results from the USAFA are in good agreement with the flight-test data, although the predicted velocity is somewhat low between $z = 8$ mm (0.3 in.) and the edge of the rake. The KTH/FOI solutions do not exhibit this behavior, but underpredict the velocity to a greater extend than the USAFA for z less than about 15. They also do not show the jet-type flow velocity profile observed in flight

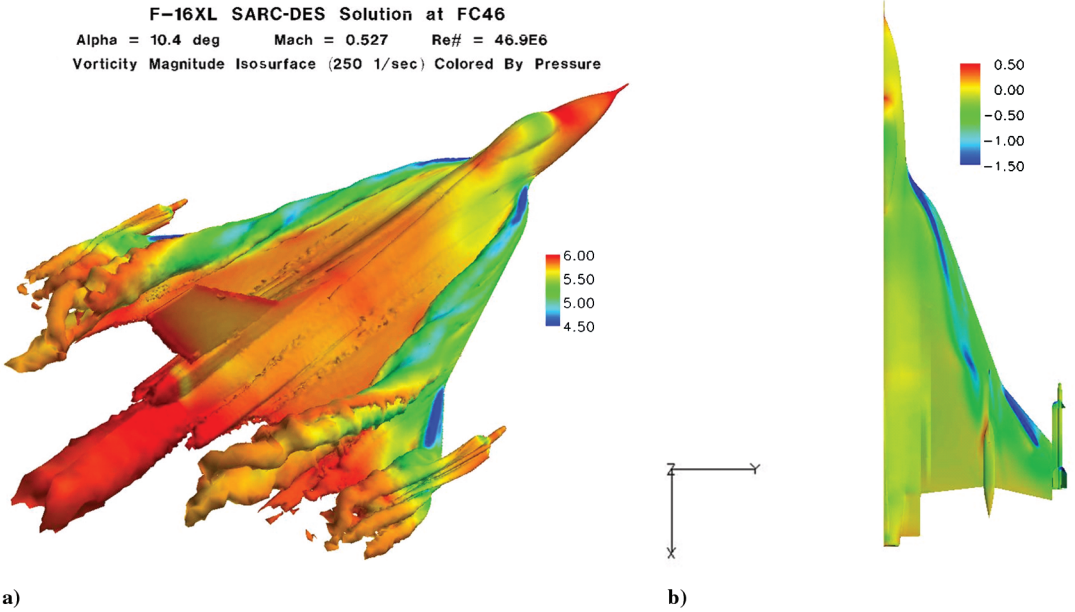

a) **b)**

Fig. 10 Flight condition 46: a) isosurfaces of vorticity magnitude colored by pressure; b) surface pressure coefficient distribution, C_p.

and are thus not as good as those obtained with k–ω EARSM shown in Fig. 6b. The hybrid and DDES modeling approaches do not improve the comparison with the measured data over standard DES, suggesting that the difference between the USAFA and KTH/FOI results are due to numerical rather then physical modeling. Results from the USAFA show small levels of unsteadiness for this rake location, as measured by the difference between minimum and maximum scaled velocity and the mean scaled velocity (Fig. 8b).

At rake 5, the benefits of the hybrid and DDES modeling approaches start to become apparent (Fig. 7c). Both approaches predict velocity profiles for this rake location that are significantly different from those predicted with standard DES and that are in much better agreement with the measured data. The DDES result leads to very good agreement with the measured data, while both standard DES solutions resemble a fuller, turbulent-type profile. An increase in the unsteadiness of the data is observed for this rake in Fig. 8c.

A similar situation is observed at rake 7 in Fig. 7d. Both the hybrid and DDES models predict velocity profiles that are in better qualitative and quantitative agreement with the measured data. For

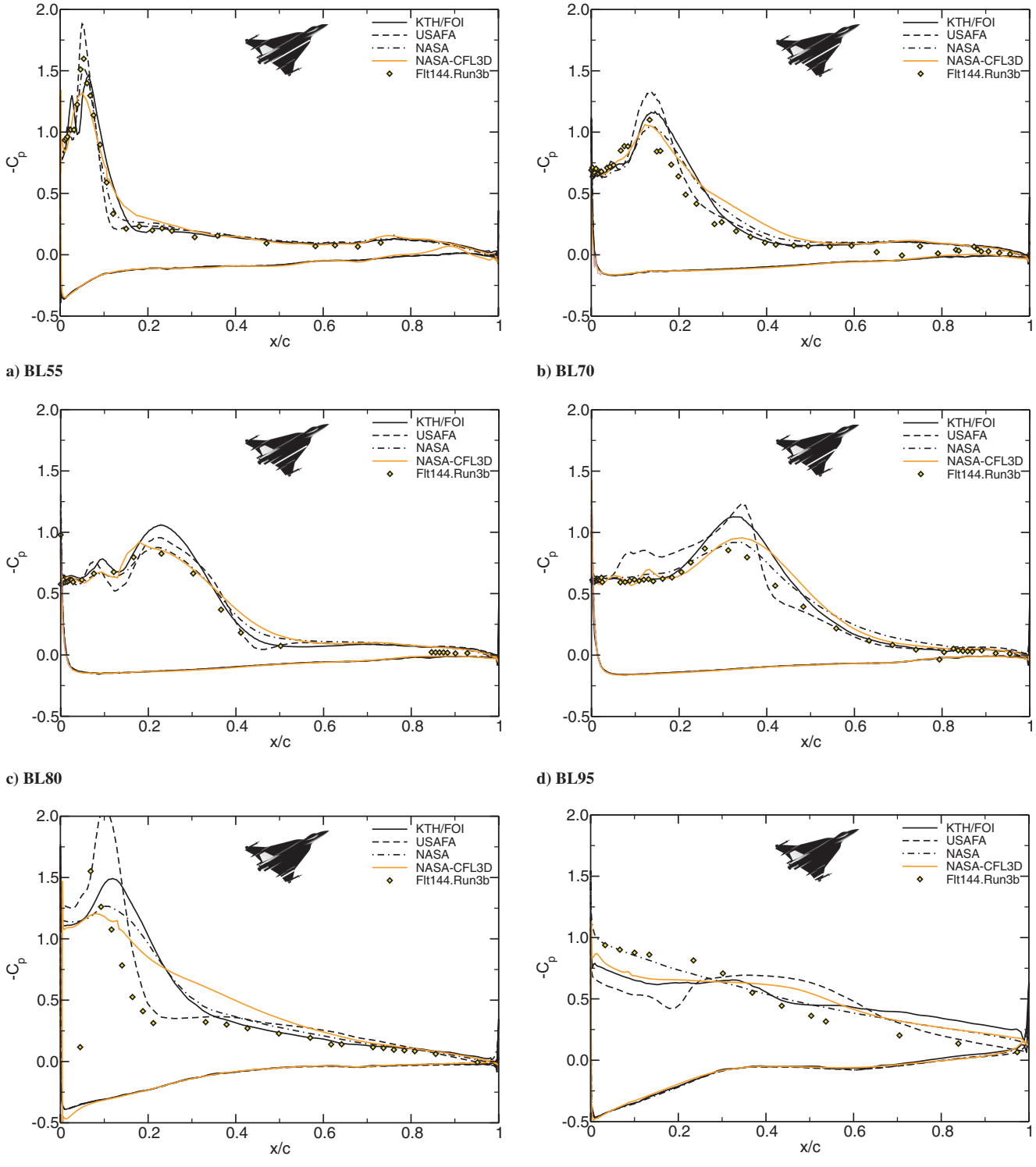

Fig. 11 Surface pressure coefficient for FC46 at various butt line stations, compared to flight-test data ($M_\infty = 0.527$, $\alpha = 10.4$ deg, and $Re = 46.9 \times 10^6$).

this location, however, the hybrid model by KTH/FOI matches the measurements best. In contrast to the KTH/FOI DES result, the USAFA DES result exhibits strong jetlike behavior, making it difficult for the DDES model to recover the true velocity profile. Overall, at rake 7 the scatter between the two DES solutions, the DES and hybrid and DDES solutions, and the flight-test data is at its worst. This is associated with the highest levels of unsteadiness for all four rakes as shown in Fig. 8d. Note that rake 7 is located in a very challenging flow region from a numerical point of view due to secondary separation occurring somewhere near the rake location due to the adverse pressure gradient the flow encounters in the spanwise direction. If the turbulence model predicts secondary separation to occur either inboard or outboard of the rake location, the corresponding velocity profiles at the rake location may have very different character. Also note that standard DES may switch from RANS to LES in the boundary layer in this region, an unwanted behavior that is known to occur in computations of flows with pressure-induced separation [34]. This problem of standard DES is addressed by the DDES and hybrid RANS-DES models.

In summary, the unsteadiness increases in regions of the secondary attachment line and under the secondary vortex and this is where the hybrid and DDES models are better than their standard DES forerunner.

2. *Flight Condition 19*

Flight condition 19 is at an angle of attack of 11.85 deg, a Mach number of 0.36, and an altitude of 10,000 ft, resulting in a Reynolds number of 46.8×10^6. This condition was chosen for comparison due to the availability of skin friction data across the left wing near FS330, which was determined with 16 modified Preston tubes in flight. The tubes were aligned with the local flow by using the same initial NASA CFL3D solution with the wall-function model at FC7 that was used to determine the boundary-layer rake orientations. The experimental c_f values were calculated from the pressure change between the total- and static-pressure tubes.

The flowfield and surface pressure distribution over the F-16XL at FC19 is not shown here because the dominant features of the flowfield at FC19 are the same as in FC7 with only minor differences due to the very similar flight conditions.

The comparison of the local skin friction values along FS330 is shown in Fig. 9. There is a large scatter in the different numerical results, both in terms of the peak skin friction coefficient underneath the primary vortex and the spanwise distribution. The magnitude of the peak c_f value is overpredicted by the linear k–ε model (NASA), while it is underpredicted by both the USAFA and KTH/FOI, with the Cobalt predictions with DES being lower than those from Edge with the Hellsten k–ω EARSM model. Quantitatively, the magnitude of the primary skin friction coefficient peak computed with Cobalt is 22% lower than the flight-test data. The predictions by NASA and KTH/FOI yield a somewhat more inboard location of the peak, whereas the location predicted by USAFA is in very good agreement with the measurements, although its associated peak value is the smallest of the three. This is clearly related to the prediction of the location of the primary vortex, which is influenced by the strength and spanwise location of the secondary vortex, which in turn depends on the interaction of the primary vortex with the boundary layer and thus the turbulence model. The width of the footprint of the primary vortex in the skin friction distribution is very well predicted by the DES of the USAFA, whereas the KTH/FOI and NASA predictions show a wider footprint. With regards to the local skin friction underneath the secondary vortex, the DES results of the USAFA agree very well with the measured values, as do those of KTH/FOI. The unsteady bounds computed for c_f by the USAFA (Fig. 20 of [4], not shown here) indicate high levels of unsteadiness underneath the secondary vortex. The jagged curve predicted by USM3D (NASA), with skin friction levels being too high, indicates a problem which may be related to the convergence of the solution or the fact that there are highly stretched tetrahedral elements in the viscous region of the grid used by NASA. Note that both the results of NASA and KTH/FOI show an anomaly or peak in the skin friction distribution between $2y/b_{\text{local}} = 0.5$ and 0.6 (BL50-65), inboard of the primary vortex, which is not present in the flight data. The USAFA results do not display this behavior despite the fact that they were computed on exactly the same grid as that employed by KTH/FOI. The origin of this anomaly seems to be related to a surface discontinuity retained by those participants that used the original surface grid but removed by others. This discontinuity, really a streamwise depression of small width and depth, seems to be the cause of the predicted behavior. Overall, the wall-resolved computational results are in better agreement with the measured data than the CFL3D results with wall functions.

KTH/FOI also observed significant differences in terms of the predictive capability of different turbulence models, as demonstrated in [3]. The results obtained with the DRSM were in best agreement with the measured c_f values. The primary peak skin friction value was predicted within 2% of the measured data with this model and the spanwise location matched the measured one; however, the secondary peak was somewhat overpredicted. The k–ω EARSM predicted a slightly lower peak value under the primary vortex, as

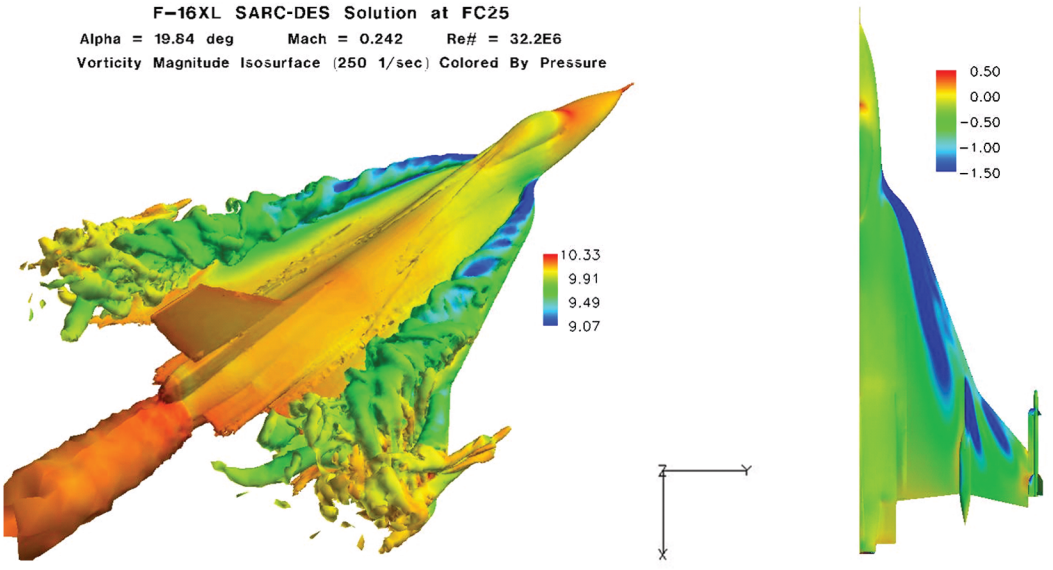

a) b)

Fig. 12 Flight condition 25: a) isosurfaces of vorticity magnitude colored by pressure; b) surface pressure coefficient distribution, C_p.

shown in Fig. 9. The Spalart–Allmaras model, however, failed to predict both the peak value under the primary vortex and the region of high skin friction under the secondary vortex. It was also found that the rotational correction improved the predictive capability of the k–ω EARSM underneath the primary vortex but worsened that of the Hellsten k–ω EARSM.

3. *Flight Condition 46*

Flight Condition 46 is at an angle of attack of 10.4 deg, a Mach number of 0.527, and an altitude of 24,000 ft, resulting in a Reynolds number of 46.9×10^6. This condition was chosen for comparison due to the availability of surface pressure distribution data. Figure 10 depicts the flowfield over the F-16XL at FC46. As in FC7, isosurfaces of vorticity magnitude of 250 1/s colored by pressure are shown in the perspective view (Fig. 10a) and surface C_p for the right wing is shown in the planform view (Fig. 10b). The dominant features of the flowfield are the same as in FC7 with only minor differences, because the Reynolds number is nearly identical and compressibility effects are probably not important.

Figure 11 is used to compare the flight-test surface pressure coefficient data with numerical results for FC46 at six different BL

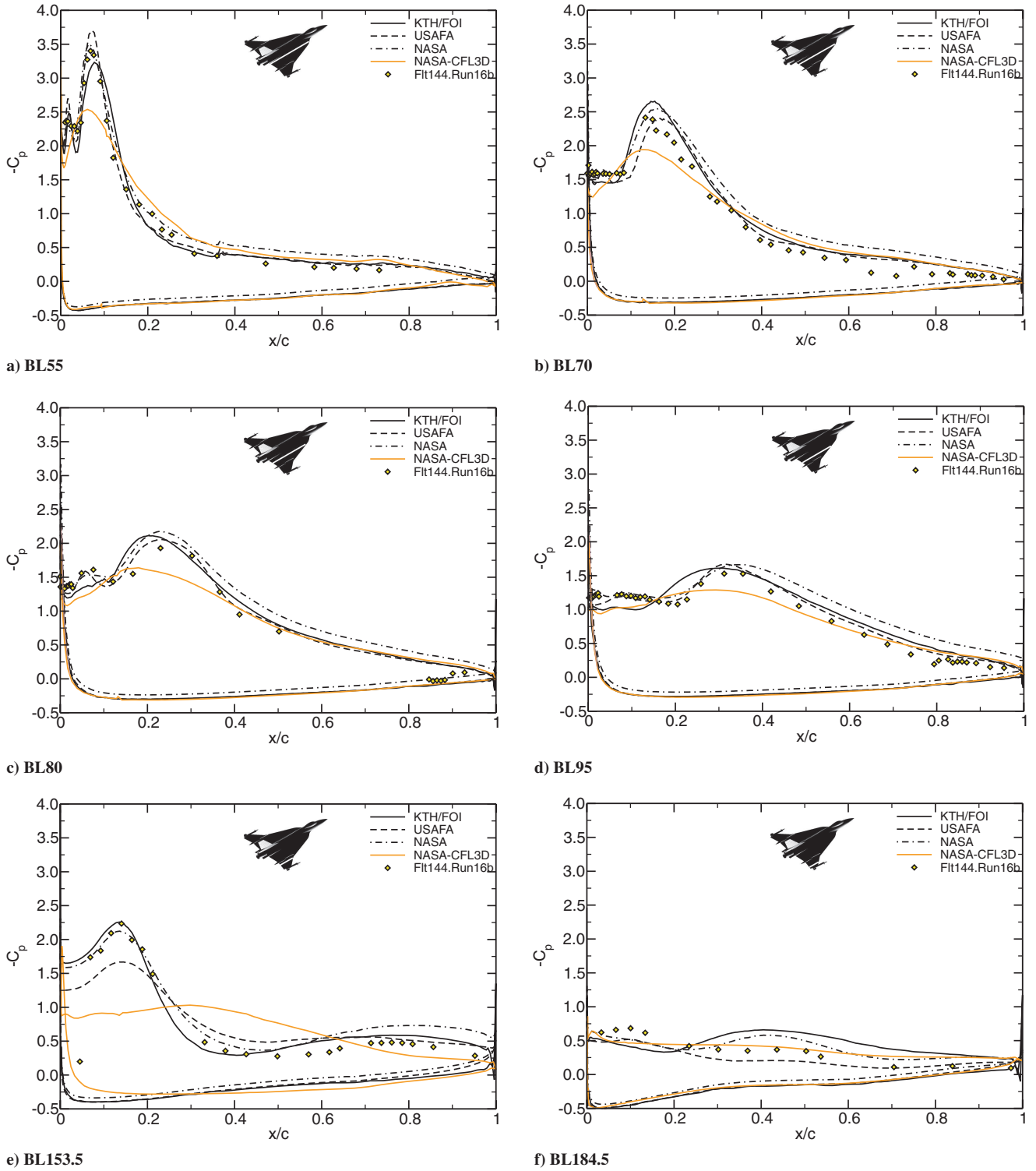

Fig. 13 Surface pressure coefficient for FC25 at various butt line stations, compared to flight-test data ($M_\infty = 0.242$, $\alpha = 19.84$ deg, and $Re = 32.22 \times 10^6$).

positions. It demonstrates that the main C_p features, including suction peaks, are generally well predicted, both chordwise and spanwise, but not in all details. The primary suction peak heights are consistently overpredicted by time-averaged DES (USAFA), apart from BL184.5, and by the Hellsten k–ω EARSM (KTH/FOI) for BL80, 95, and 105 (BL105 not shown here). The chordwise location of the suction peak under the primary vortex outboard of the crank is predicted too far downstream/inboard (BL153.5) by all models; only the DES and wall-function models predict the location of the suction peak somewhat closer to the leading edge. The magnitude of the suction peak at BL153.5 is approximately predicted by the Hellsten k–ω EARSM, while the other models feature a significantly higher or lower value. The secondary suction peaks, on the other hand, are very well predicted by the linear k–ε model (NASA), the wall-functions

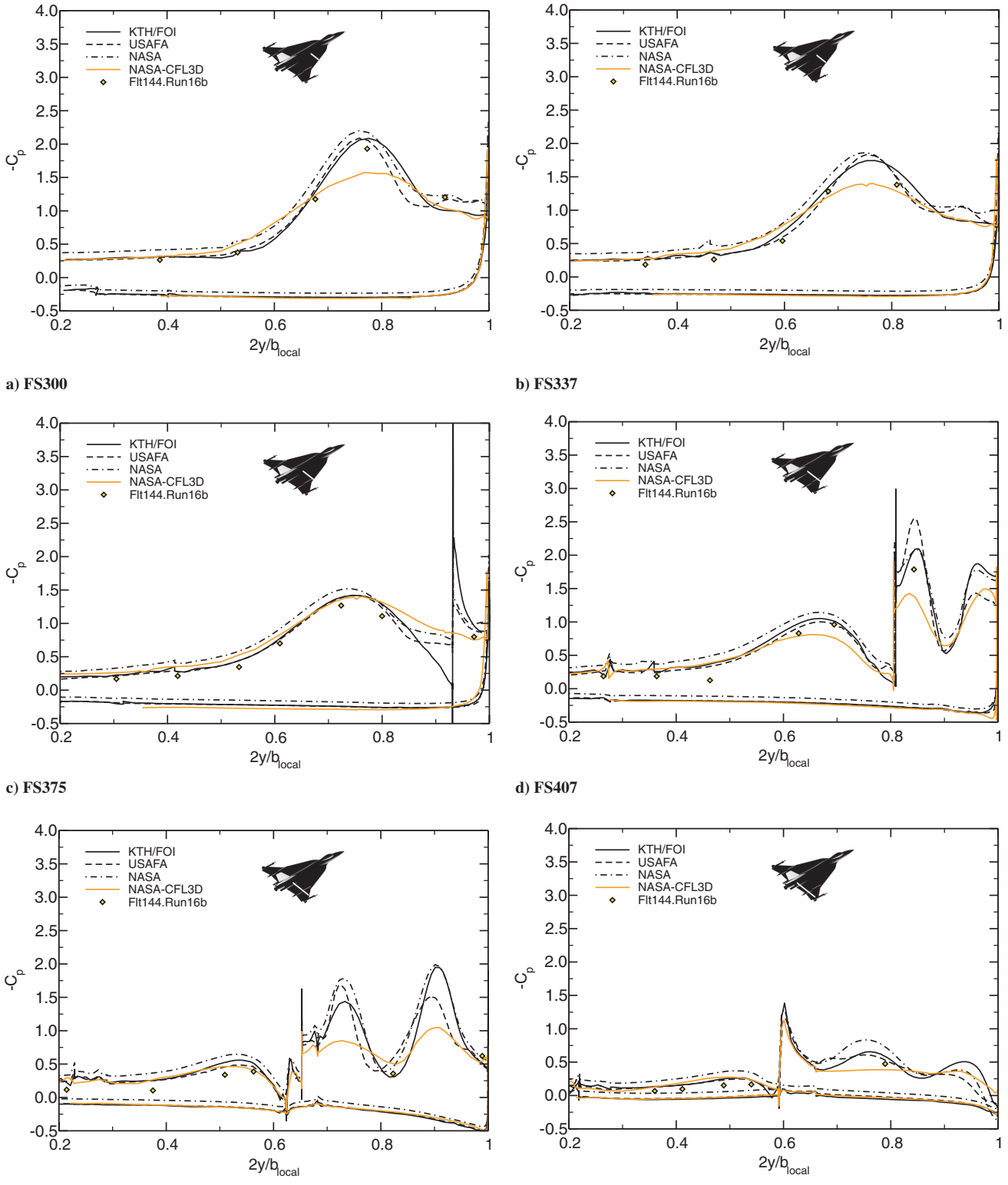

a) FS300 b) FS337

c) FS375 d) FS407

e) FS450 f) FS492.5

Fig. 14 Surface pressure coefficient for FC25 at various fuselage stations, compared to flight-test data ($M_\infty = 0.242$, $\alpha = 19.84$ deg, and $Re = 32.22 \times 10^6$).

model, and the Hellsten k–ω EARSM at BL70, 80, and 95. At BL55, however, Hellsten k–ω EARSM predicted a stronger secondary vortex, which effectively displaced the primary wing vortex, resulting in a lower primary suction peak on the surface. At BL95 the magnitude of the average primary and secondary suction peak heights computed with DES are significantly higher than the measured ones, probably indicating inadequacies with the switch from RANS to DES, which can take place somewhere inside the boundary layer and produce premature (grid-induced) separation, leading to a stronger secondary vortex. DDES could be a remedy for this problem. DES also predicted a much narrower primary vortex footprint than the other models. The C_p distributions predicted with the USM3D linear k–ε model are very similar to those predicted by the CFL3D wall-functions model and are in good agreement with the measured data at BL70, 80, 95, and 184.5. It is interesting to note, however, that in the region of anticipated flow unsteadiness close to the wing-tip missile (BL184.5) the linear k–ε model outperforms the other models, even DES. The scatter between the different turbulence models is rather significant for this BL. The BL184.5 computational data by the USAFA [4] showed significant unsteadiness as in the FC7 case with the majority of the data within the minimum and maximum C_p bounds of the computational data; however, DES misses the inboard trend of a higher C_p (not shown). Again, it would be of interest to evaluate the performance of DDES for this flow condition.

No firm conclusions could be made regarding the predictive capability of the different turbulence models in the turbulence model study by KTH/FOI [3] (not shown here). The Spalart–Allmaras one-equation model, however, was generally seen to predict lower and wider suction peaks than the other models and the agreement with the measured data was rather poor. The DRSM was seen to predict the highest suction peaks, followed by DES. Almost no difference could be seen between the curvature-corrected and the uncorrected EARSM, but all EARSM models showed a stronger secondary vortex, which displaced the primary vortex as seen in the Hellsten k–ω EARSM results for BL55 in Fig. 11a. This behavior was also seen by NASA with the nonlinear two-equation model. The differences between models were observed to be rather large in BL184.5 where the flow is affected by the vicinity of the sidewinder missile and is probably very chaotic. An interesting finding was that the increased modeling complexity of DRSM and DES did not pay off in terms of the quality of the result for this flight condition.

The turbulence modeling study by NASA [5] (not shown here) concluded that there seemed to be a slight advantage to using the two-equation nonlinear k–ε turbulence model with respect to predicting C_p, at least for the USM3D solver and for this flight condition. The two-equation linear k–ε model was deemed slightly better than the Spalart–Allmaras model and almost as good as the nonlinear one. Similar to the findings by KTH/FOI, the NASA results with the Spalart–Allmaras model also show lower and wider suction peaks

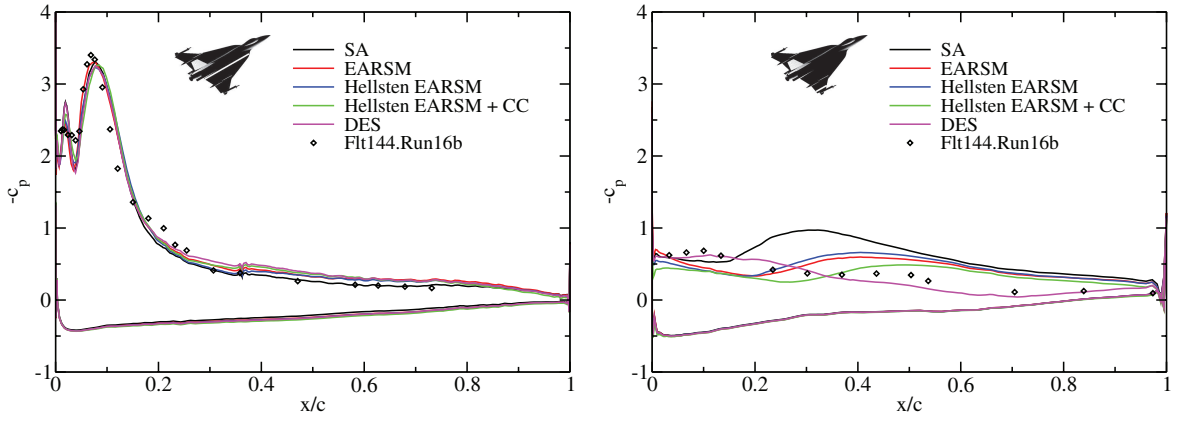

a) BL55 b) BL184.5

Fig. 15 Surface pressure coefficient for FC25, different turbulence models, Görtz and Jirásek [3] ($M_\infty = 0.242, \alpha = 19.84$ deg, and $Re = 32.22 \times 10^6$).

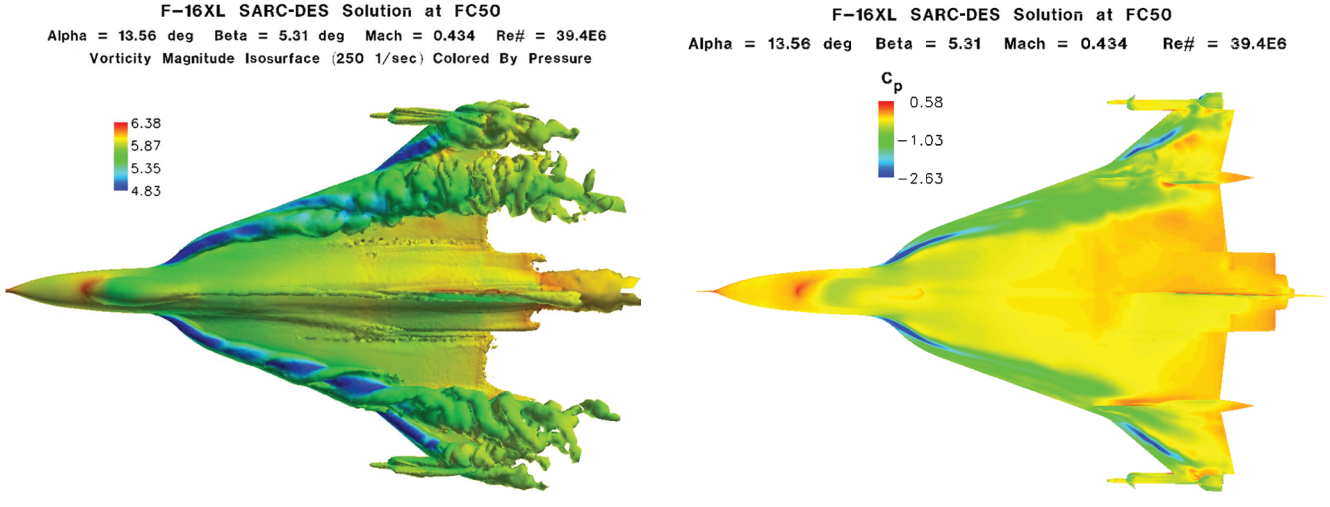

a) b)

Fig. 16 Flight condition 50: a) isosurfaces of vorticity magnitude colored by pressure; b) surface pressure coefficient distribution, C_p.

than the other two models and the agreement with the measured data was rather poor.

B. Results at High Angle-of-Attack Flight Condition Without Sideslip (FC25)

Flight condition 25 is for a higher angle of attack of 19.84 deg, a Mach number of 0.242, and an altitude of 10,000 ft, resulting in a Reynolds number of 32.2×10^6. This condition was considered by the CAWAPI RTO Task Group because better defined vortical flow features could be expected over the upper surface, perhaps even vortex breakdown or vortex unsteadiness over the aft portion of the aircraft. Large scale flow unsteadiness is also associated with such phenomena and hence this may be a good case study for gauging the differences between the physical modeling of steady RANS and DES, compared with flight data.

Figure 12 depicts the flowfield over the F-16XL at FC25. Isosurfaces of vorticity magnitude of 250 $1/s$ colored by pressure are

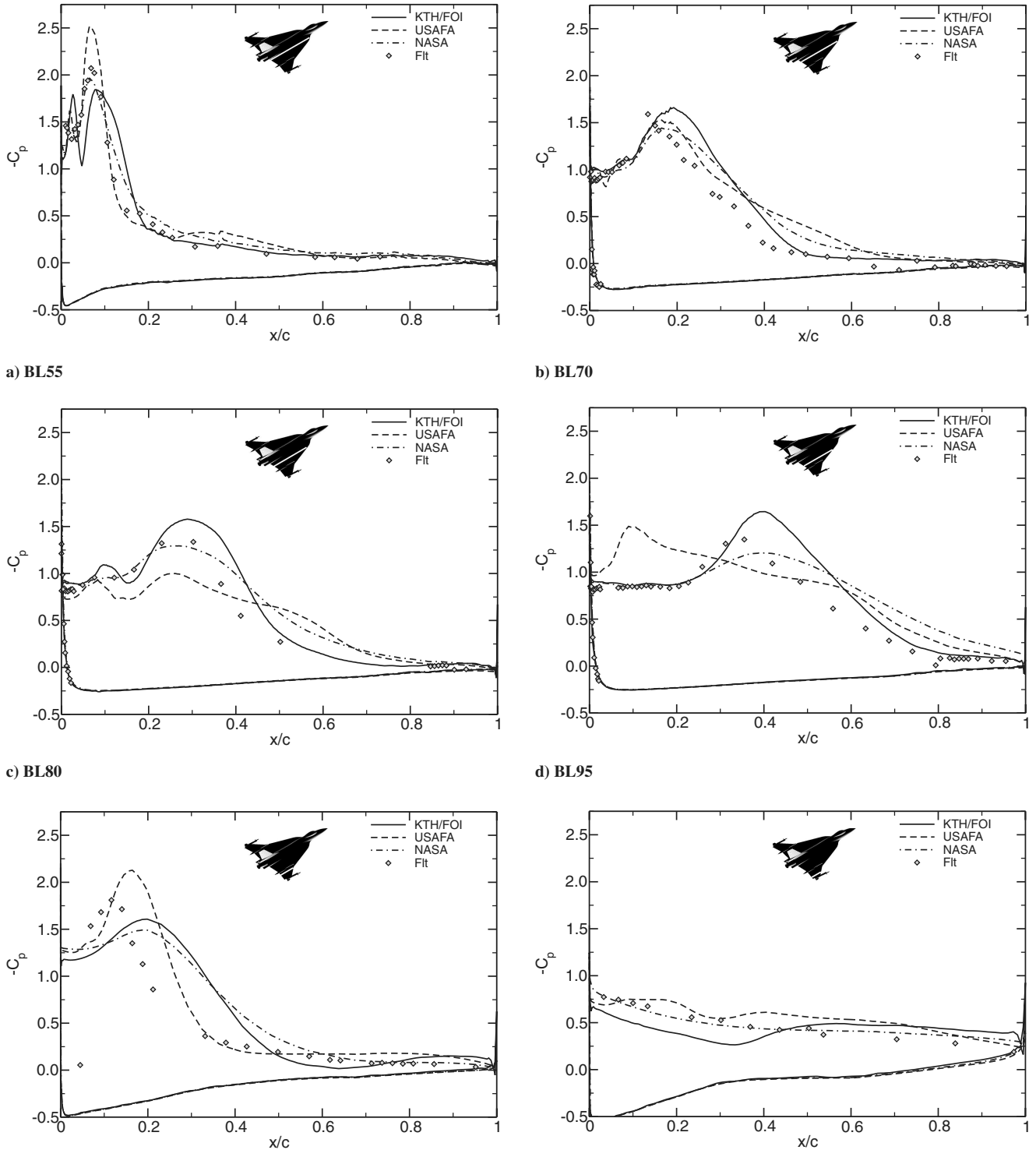

a) BL55 b) BL70

c) BL80 d) BL95

e) BL153.5 f) BL184.5

Fig. 17 Surface pressure coefficient for FC50 at various butt line stations, compared to flight-test data ($M_\infty = 0.434$, $\alpha = 13.56$ deg, $\beta = +5.31$ deg, and $Re = 39.41 \times 10^6$).

shown in the perspective view (Fig. 12a) and surface C_p for the right wing is shown in the planform view (Fig. 12b). As in the case of FC7, it is apparent that the dominant features of the flowfield are the leading-edge vortex, the air-dam vortex, the outer-wing vortex, and a complicated set of vortices from the AIM-9 fins and forebody. However, the increased angle of attack is predicted to cause the breakdown of these vortices to occur farther forward creating a more significantly unsteady flowfield. It is easier to label this classic vortex breakdown due to the predicted breakdown position being well forward and inboard of the air dam/actuator pod.

Figure 13 presents a comparison of the measured C_p data with the solutions computed with DES (USAFA), the Hellsten k–ω EARSM (KTH/FOI), the linear k–ε model (NASA), and the wall-functions model (NASA CFL3D) for FC25 at various BL positions. The overall agreement with the experimental data is very good for this flight condition; only the wall-function model consistently

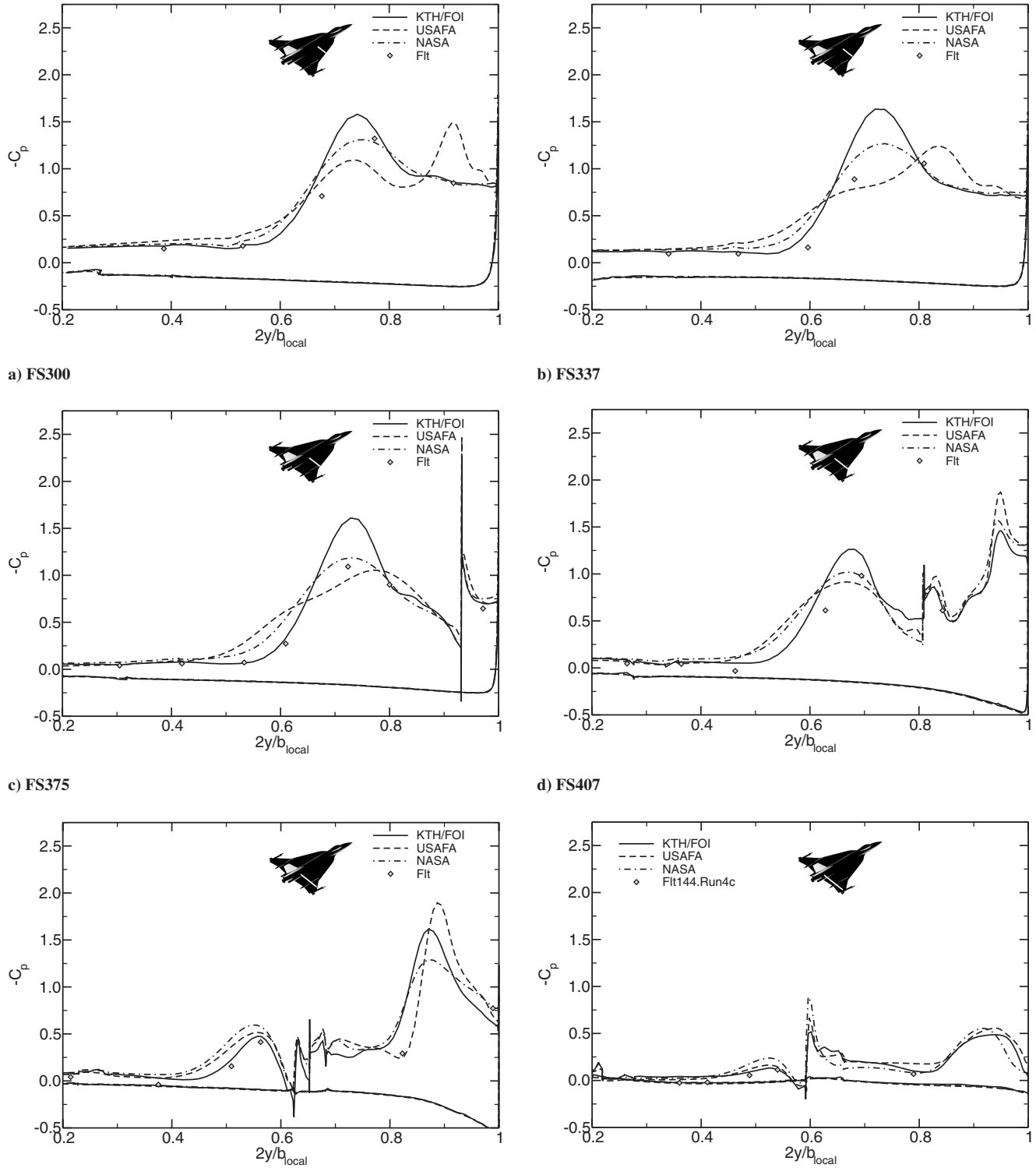

a) FS300 **b) FS337**

c) FS375 **d) FS407**

e) FS450 **f) FS492**

Fig. 18 Surface pressure coefficient for FC50 at various fuselage stations, compared to flight-test data ($M_\infty = 0.434$, $\alpha = 13.56$ deg, $\beta = +5.31$ deg, and $Re = 39.41 \times 10^6$).

underpredicts the magnitude of the primary and secondary vortices with locations too far inboard. All other models perform equally well, both in predicting the magnitude and location of the primary and secondary suction peaks, with the following exceptions: At BL153.5 DES predicts a lower primary suction peak than the other models. The EARSM predicts a primary suction peak that is somewhat too broad but of the correct magnitude (except for BL184.5), and a weaker footprint of the secondary vortex.

Figure 14 presents similar data for various FS positions at FC25. As is true of all BL positions, the computed surface pressure data at all FS positions are in excellent agreement with the available flight-test data. There is conflicting and nonconclusive evidence as to whether vortex breakdown occurs over the wing.

KTH/FOI concluded from their turbulence modeling study [3] that, compared to the medium-angle-of-attack flight conditions, the differences between turbulence models grew larger at FC25, with the exception of BL55, which is shown in Fig. 15a. Note that the primary suction peak is well predicted despite the fact that some models overpredicted the strength of the secondary vortex, which has a displacing effect on the primary vortex. Results obtained using the

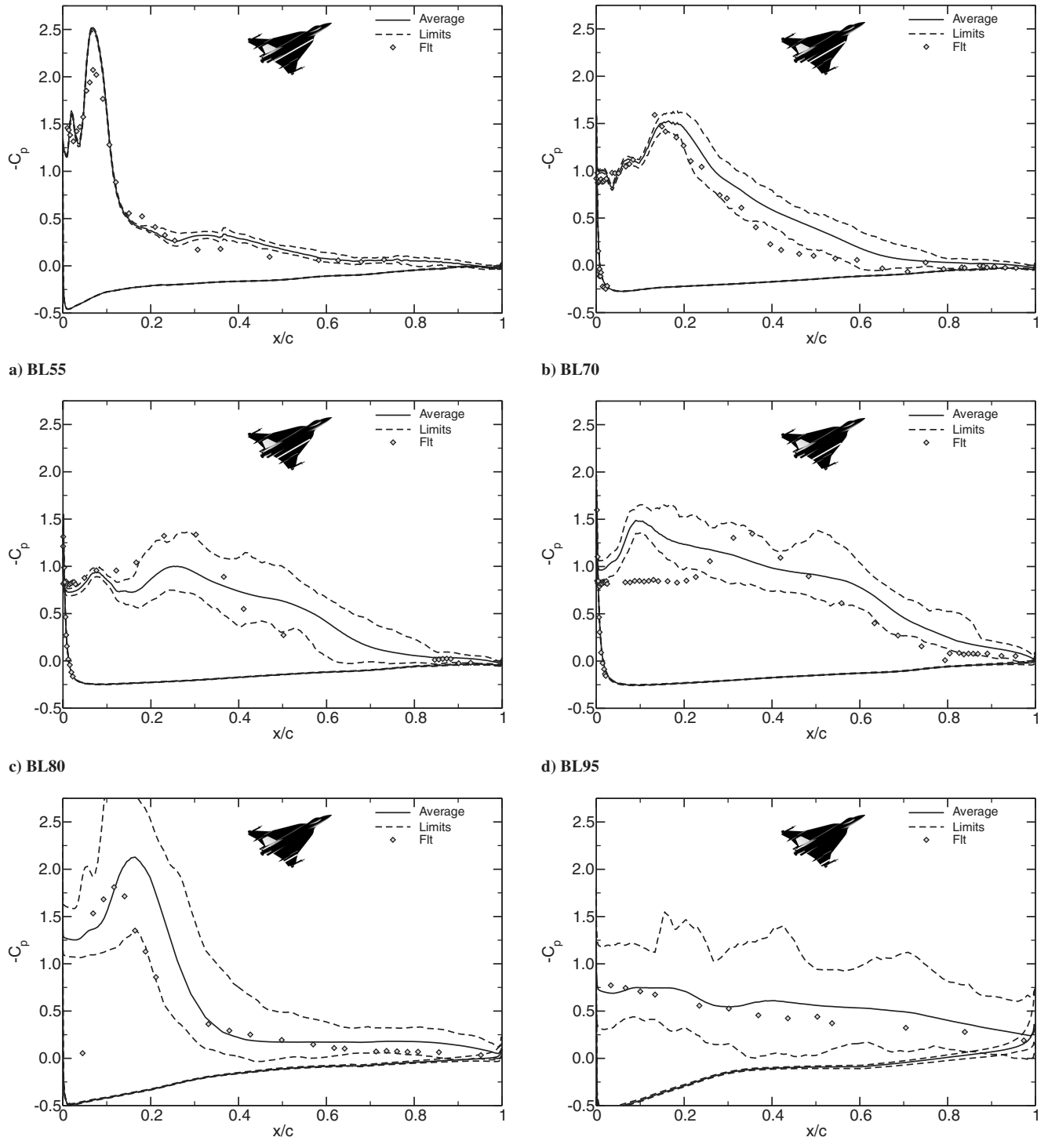

Fig. 19 Computed average surface pressure coefficient and unsteady bounds from DES for FC50 at various butt line stations, compared to flight-test data ($M_\infty = 0.434$, $\alpha = 13.56$ deg, $\beta = +5.31$ deg, and $Re = 39.41 \times 10^6$).

Spalart–Allmaras model departed quickly from those obtained using the other models and overpredicted the height of the primary suction peak throughout. All models apart from the Spalart–Allmaras model agreed very well with the measured data at BL153.5, which is outboard of the crank. From the family of EARSM models it was the Hellsten k–ω EARSM with rotational corrections (RC) that showed the best prediction of both primary and secondary suction peaks. The only position where the Hellsten k–ω EARSM + RC model showed a different behavior compared to the flight-test data was in BL184.5, as shown in Fig. 15b. Only DES predicted the C_p distribution qualitatively and quantitatively at BL184.5. It turned out that the flow was separated and unsteady there, and that the higher modeling complexity of DES paid off in predicting the correct trend in a time-averaged sense. This model was also superior to the other models in predicting the secondary suction peak at BLs 70, 80, and 95. In addition, it was better at predicting consistently the spanwise/chordwise position of the primary vortex; however, the peak suction was somewhat too low.

In [4] the USAFA showed that unsteady effects were minimal for BL40–BL70 and FS185, whereas the plots with unsteady bounds showed measurable unsteadiness for BL80, BL95, BL105, FS337.5, and 375, and significant unsteadiness in the surface C_p for BL127.5, BL153.5, BL184.5, and all FS positions aft of and including FS407.5. Similarly, KTH/FOI [3] also showed that the unsteadiness was located over the rear of the wing, close to the wing tip, which explains why DES performed better than the RANS models at BL184.5.

Overall, there is excellent agreement with the flight-test data for this flight condition and the comparison shows the utility of hybrid turbulence models and reliable CFD solvers to compute these complex unsteady fighter flowfields at high α.

C. Results at Sideslip Flight Conditions (FC50, 51)

There are two flight conditions with nonzero sideslip angles, medium angles of attack, and subsonic Mach numbers. These two conditions have sideslip angles of +5.31 deg (FC50) and −4.58 deg (FC51). Solutions were computed for these two conditions with a mirrored full-span grid based on the original half-span grid used in all of the previously discussed computations. This section presents results for these two nonsymmetric flight conditions.

1. *Flight Condition 50*

Flight condition 50 is at a sideslip angle β of +5.31 deg, an angle of attack of 13.56 deg, a Mach number of 0.434, and an altitude of 24,000 ft resulting in a Reynolds number of 39.4×10^6. Figure 16 depicts the flowfield over the F-16XL at FC50. Isosurfaces of vorticity magnitude of 250 1/s colored by pressure are shown in the left view (Fig. 16a) and surface C_p is shown in the right view (Fig. 16b). The dominant flow features over the left wing are similar to those at FC7 but the right wing has additional vortical structures. The effect of a positive sideslip angle is an increase in the effective angle of attack and a reduction in the leading-edge sweep angle of the right wing. The increased effective angle of attack causes breakdown to occur further forward on the wing and the reduced sweep angle causes the double vortex observed by researchers performing studies of lower sweep delta wings [36].

Figures 17 and 18 depict the right wing flight-test C_p data compared to the computed results for FC50 at various BL positions and FS stations. It should be noted that for FC50 the comparison data are on the wing with the highest degree of unsteadiness due to the increased effective angle of attack and the reduced leading-edge sweep. In general, the scatter between the results produced with the three different codes is larger for this flight condition than for the previous ones. No clear trend can be observed as to which turbulence model or flow solver is superior in predicting this sideslip case. DES (USAFA) both overpredicted (BL55 and BL153.5) and underpredicted (BL80) the primary suction peak heights, while it failed to predict any suction peak underneath the primary vortex in BL95, where a very strong suction peak is located underneath the presumed location of the secondary vortex close to the leading edge instead. Surprisingly, in BL184.5, where unsteady effects are presumed to be largest, the linear k–ε model (NASA) outperformed DES (Fig. 17f), at least in a time-averaged sense. The linear model is also very good at predicting the secondary suction peaks at BL55–BL95. The Hellsten k–ω EARSM (KTH/FOI), on the other hand, overpredicted this feature in BL55 and 80 as did DES in BL55 through 95. The recovery from the strong suction peaks is not well predicted by any of the models, with the linear k–ε model giving the flattest C_p distribution. All three models suggest a significant downstream/inboard shift of the primary suction peak in BL70, BL95, and BL153.5, raising the question about uncertainties in the inflow conditions. Overall, these comparisons with flight-test data are considered fair when considering the extent of unsteady, massively separated flow over the right wing.

From Fig. 18 it is also noted that there is considerable scatter between the numerical results. Results obtained using the linear k–ε model (NASA) compare somewhat more favorable with the experimental data than those from other models, but the recovery from the suction peaks is not as good as that predicted with the Hellsten k–ω EARSM (KTH/FOI).

To assess the effect of unsteadiness on the surface pressure distribution, the time-averaged DES data by USAFA with their upper and lower unsteady bounds are compared in Fig. 19 with flight data for FC50 at the same butt lines as before. Note that the minimum or maximum values may occur at a single instance in

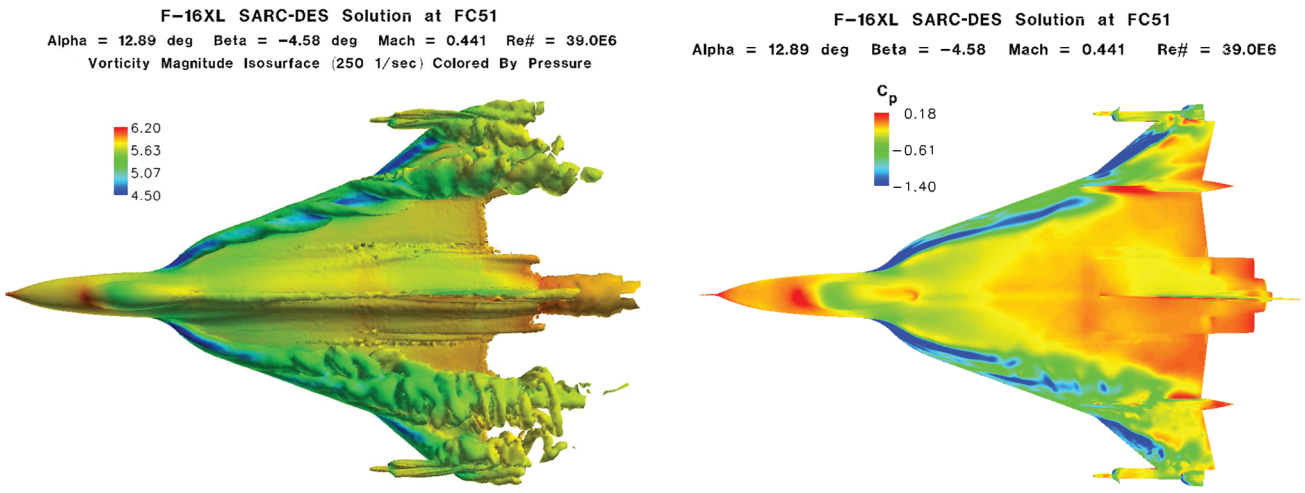

a) b)

Fig. 20 Flight condition 51: a) isosurfaces of vorticity magnitude colored by pressure; b) surface pressure coefficient distribution, C_p.

time during the entire simulation, whereas the average is generated over time. In other words, the solution can spend a longer time at intermediate values, resulting in a nonsymmetric min–max average. The BL40 and BL50 plots (not shown) indicate that unsteady effects are minimal for these inboard stations. Unlike FC7, FC19, FC46, or even FC25, FC50 shows significant unsteadiness for BL70–BL184.5 for the reasons discussed above. The BL70–BL184.5 flight-test data reside primarily inside the computed unsteady C_p bounds. Note that in BL95, Fig. 19d, where there is no primary suction peak underneath the primary vortex in a time-averaged sense, the experimental suction peak values reside inside the unsteady DES bounds; however, there is a region ahead of the primary suction peak that is overpredicted by the computations, as discussed above.

2. *Flight Condition 51*

Flight condition 51 is at a sideslip angle β of -4.58 deg, an angle of attack of 12.89 deg, a Mach number of 0.441, and an altitude of 24,000 ft, resulting in a Reynolds number of 39.0×10^6. Figure 20 depicts the flowfield over the F-16XL at FC51. Isosurfaces of vorticity magnitude of 250 1/s colored by pressure are shown in the

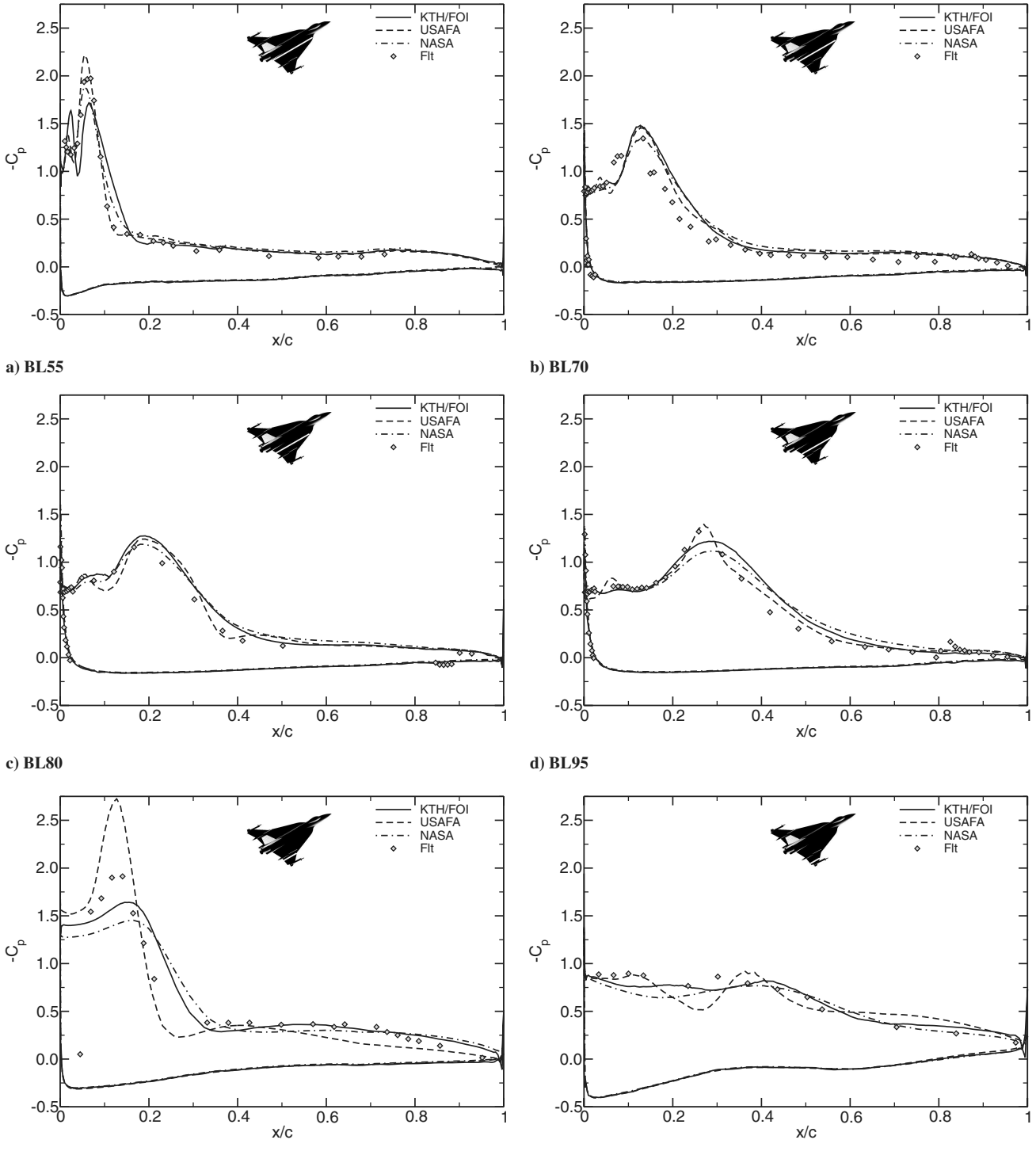

Fig. 21 Surface pressure coefficient for FC51 at various butt line stations, compared to flight-test data ($M_\infty = 0.441$, $\alpha = 12.89$ deg, $\beta = -4.58$ deg, and $Re = 38.96 \times 10^6$).

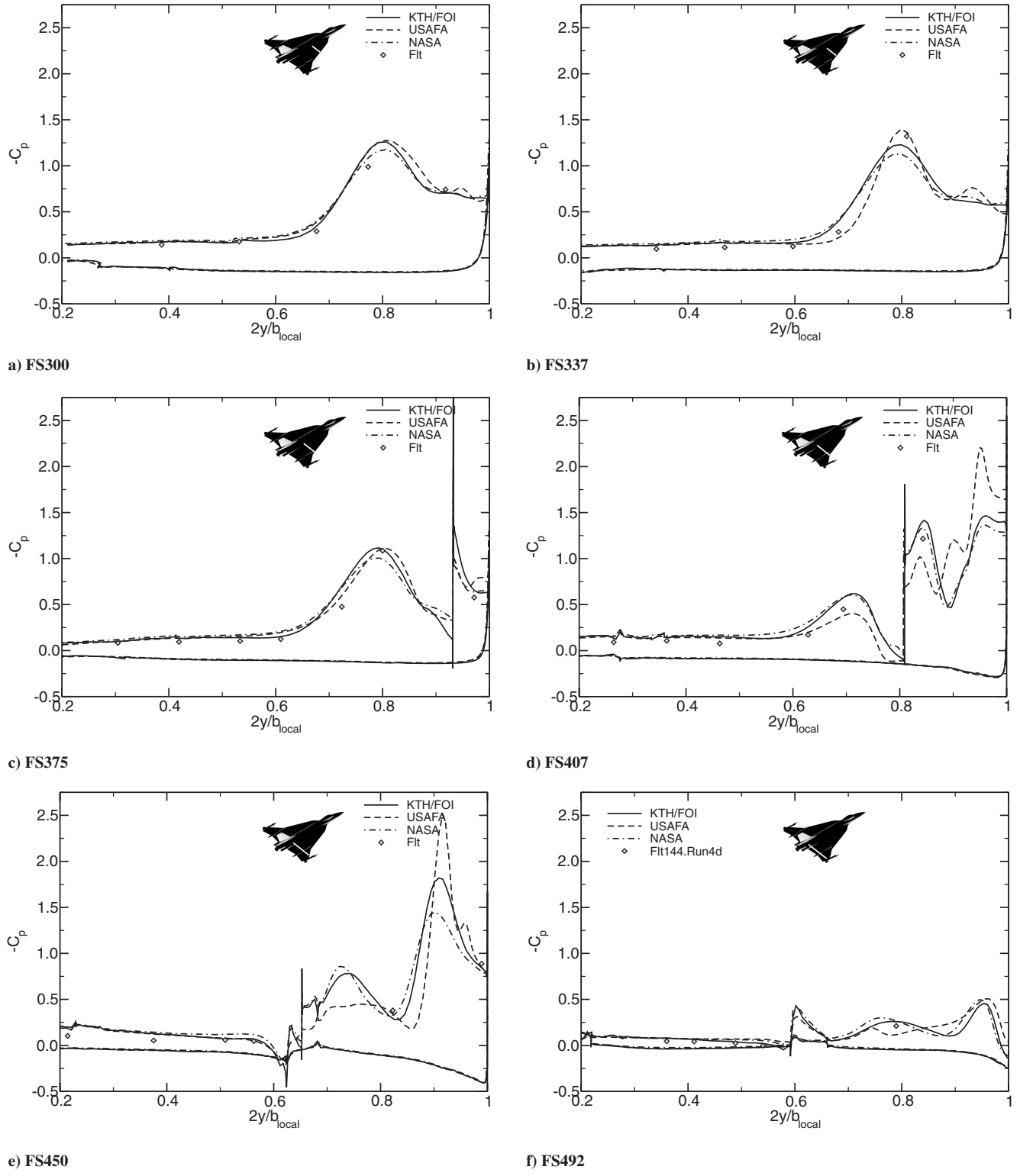

a) FS300 b) FS337

c) FS375 d) FS407

e) FS450 f) FS492

Fig. 22 Surface pressure coefficient for FC51 at various fuselage stations, compared to flight-test data ($M_\infty = 0.441, \alpha = 12.89$ deg, $\beta = -4.58$ deg, and $Re = 38.96 \times 10^6$).

left view (Fig. 20a) and surface Cp is shown in the right view (Fig. 20b). Because the flight conditions of FC51 are nearly the same as FC50 but with an opposite sideslip, the discussions above hold for FC51 but for the opposite wing.

Figures 21 and 22 depict the flight-test C_p data compared to the numerical results for FC51 at various BL positions and FS stations. It should be noted that for FC51 the comparison data are on the wing with the lowest degree of unsteadiness due to the decreased effective angle of attack and the increased leading-edge sweep. For this reason, the scatter between the three different turbulence models is considerably less than for FC50. The overall agreement with the measured data is good, except for BL153.5, where the primary suction peak is overpredicted by DES (USAFA) and underpredicted by the two RANS models. The suction peak predicted by the RANS models is located slightly inboard of the measured data at this BL and BL95. The agreement between DES and the sharp peak in the flight-test data in BL95 in Fig. 21d is remarkable, because the RANS models predict a flattened pressure distribution with a lower suction

peak. Finally, at BL184.5, where unsteady effects are anticipated to be strongest, all models predict the surface pressure distribution qualitatively, but not quantitatively.

As for all but two BL positions, the C_p data predictions at all FS positions are in good agreement with the available flight-test data.

D. Discussion

Although the agreement between the three codes was generally good, the differences seen in the results between the codes can be attributed to a combination of code-specific and grid-specific differences.

The code-specific differences can be classified into differences in the numerical modeling, the physical modeling, and how the results were postprocessed. The implications of the different discretization type were already discussed in the code comparison. In the tetrahedral part of the common hybrid grid used by the USAFA and KTH/FOI, the cell-centered approach implemented in Cobalt is simply expected to yield higher accuracy over the vertex-centered discretization used in the Edge code, but at a higher computational expense, whereas the differences between the two approaches are expected to be less pronounced in the prismatic layers. Because there are few prismatic layers in the grid used, the effect of the tetrahedral part of the grid may be important but difficult to quantify. Differences in the results can also be attributed to flow conditions where the flow is locally unsteady but was modeled as steady (RANS) in one code and unsteady (DES) in another. The different turbulence models used with the different codes may perform rather well in regions of attached flow. However, the flow over the present aircraft configuration features massive separation from round and sharp leading edges, air dams, and smooth surfaces, causing scatter between turbulence models in the location of separation and reattachment lines and the formation of vortices and their interaction, which in turn affects the local pressure distribution. Also, the different turbulence models may be more or less sensitive to the grid resolution, an effect that can only be investigated through thorough grid refinement studies, which were out of the scope of the present authors. Further grid-turbulence model interplay, as in the case of DES, adds to the complexity of the physical modeling effect. In terms of postprocessing, different ways of computing the skin friction coefficient in the different codes may explain some of the observed differences, but are unlikely to be the only reason.

The grid-specific differences are a result of how the boundary layer was discretized. NASA used an all-tetrahedral grid while USAFA and KTH/FOI used a hybrid grid.

Apart from the differences in the result between the three different codes, there were also cases where a general discrepancy between the measurements and the numerical results could be observed. They may be due to underresolved or unresolved flow features, which calls for grid adaptation. It is also plausible to assume that the way the flight-test data and the time-dependent numerical data were averaged was different. The assumption of symmetric flow for flight conditions with nominally zero sideslip may impact the solution when the actual sideslip angle was nonzero, although this is believed to be a slight effect. In terms of skin friction, it is well known that skin friction is one of the more challenging coefficients to match and may need additional grid resolution to improve the flight-test data comparison.

Nonetheless, in all of the areas discussed previously, progress has been made which shows up as improved solutions over those obtained a few years earlier with CFL3D. Also, as a result of the many computations with the different codes, it was demonstrated what can be achieved with state-of-the-art numerical simulations, while highlighting some of the shortcomings.

VI. Conclusions

The vortical flow over a full-scale model of the F-16XL-1 aircraft was computed for seven different flight conditions using a standard unstructured grid family and three different flow solvers, two of them cell centered, and one node centered. Steady flow solutions were obtained with several eddy-viscosity turbulence models, and algebraic and differential Reynolds-stress models. Unsteady flow computations employed a number of hybrid RANS-LES models. The CFD solutions were compared to flight-test data for the surface pressures distribution, local skin friction, and boundary-layer velocity profiles.

The overall flowfield topology was very well resolved. Primary and secondary vortices inboard and outboard of the crank of the wing were captured, as well as air-dam and missile fin vortices. DES resolved more flow features than the steady flow simulations although this was at additional computational expense. The only location where CFD consistently failed to predict the flight data, both quantitatively and qualitatively, was the outermost wing butt line where the flow is very complex and presumed unsteady due to the interaction of the primary and secondary inner wing vortices, the outboard primary and secondary vortices, the wing-tip missile vortices, and the vortices that originate from the interaction of the inboard vortices with the air dam. DES brought about some improvement in the prediction of flow at this location by quantifying the unsteady bounds, but was not consistently superior over RANS modeling in predicting the surface pressure distribution in a time-averaged sense. At moderate angles of attack, where unsteady effects are not large, the pressure distributions from eddy viscosity and Reynolds-stress models did not differ very much from the DES solutions. DES computations come at an increased cost over steady RANS computations and are clearly unnecessary for such flight conditions. In a few cases, DES even failed to predict the pressure distribution characteristics of the vortical flow at some locations on the wing. When there is a large amount of unsteady flow, however, it may be the only method of capturing the mean loads and the amplitude and frequencies of large unsteady motion, which the RANS methods are unable to capture, even in unsteady RANS mode, due to dissipation effects.

The boundary velocity profiles obtained with the RANS models of the different codes show rather good agreement with measured data at different rake locations. The DES solutions obtained with two of the codes deviate from the measured data at several rake locations. DDES and hybrid RANS-LES modeling improve upon this disadvantage of standard DES modeling.

None of the codes or turbulence models proved to be superior over the other codes or models in the moderate angle-of-attack range at subsonic speeds. It is thus not possible to provide any guidance on the best way to calculate such complex flows on the basis of the present results, despite the rather large number of computations. The use of a particular turbulence model may perhaps be motivated by the confidence of the user in the particular model and consistency of its results at different flight conditions rather then its performance at one flight condition.

Although the agreement between the three codes was generally good, the differences between the three different flow solvers using a standard grid were attributed to differences in the discretization, the physical modeling in terms of turbulence and unsteadiness, and specifics of the grid in the viscous region.

In general, the results obtained with the three different solvers using the family of common unstructured grids showed significant improvement over those obtained a few years earlier with an order of magnitude fewer grid points and with other geometry/flow-modeling differences. This shows that progress has been made in areas such as turbulence modeling, grid generation, and numerical methods that have let to greatly improved simulation capabilities for vortical flows over complex aircraft configurations.

Acknowledgments

The authors gratefully acknowledge the support provided by Lockheed Martin Aeronautics Company, Fort Worth, in providing a refined initial graphics exchange specification (IGES) geometry file and the parameter values of a generic engine that were subsequently used by facet members in their CFD studies; the geometrical work performed by Edward B. Parlette of Vigyan, Inc., in generating a series of unstructured, tetrahedral grids from the IGES file, with the last one known as the base or common unstructured grid; and the C_p

layouts and computational support provided by Alaa Elmiligui of Analytical Services and Materials, Inc.

References

[1] Lamar, J. E., Obara, C. J., Fisher, B. D., and Fisher, D. F., "Flight, Wind-Tunnel, and Computational Fluid Dynamics Comparison for Cranked Arrow Wing (F-16XL-1) at Subsonic and Transonic Speeds," NASA TP-2001-210629, 2001.

[2] Obara, C. J., and Lamar, J. E., "Overview of the Cranked-Arrow Wing Aerodynamics Project International," *Journal of Aircraft*, Vol. 46, No. 2, 2009, pp. 355–368. doi:10.2514/1.34957

[3] Görtz, S., and Jirásek, A., "Unstructured Steady/Unsteady Solutions with Edge for CAWAPI F-16XL at KTH/FOI," AIAA Paper 2007-0678, 2007.

[4] Morton, S. A., McDaniel, D. R., and Cummings, R. M., "F-16XL Unsteady Simulations for the CAWAPI Facet of RTO Task Group AVT-113," AIAA Paper 2007-0493, 2007.

[5] Lamar, J. E., and Abdol-Hamid, K. S., "USM3D Unstructured Grid Solutions for CAWAPI at NASA LaRC," AIAA Paper 2007-0682, 2007.

[6] Boelens, O. J., Badcock, K. J., Elmilgui, A., Abdol-Hamid, K. S., and Massey, S. J., "Comparison of Measured and Block Structured Simulations for the F-16XL Aircraft," *Journal of Aircraft*, Vol. 46, No. 2, 2009, pp. 377–384. doi:10.2514/1.35064

[7] Fritz, W., Davis, M. B., Karman, S. L., Jr., and Michal, T., "RANS Solutions for the CAWAPI F-16XL Using Different Hybrid Grids," *Journal of Aircraft*, Vol. 46, No. 2, 2009, pp. 409–422. doi:10.2514/1.35106

[8] Boelens, O. J., Görtz, S., Morton, S. A., Fritz, W., and Lamar, J. E., "Description of the F-16XL Geometry and Computational Grids Used in CAWAPI," AIAA Paper 2007-488, 2007.

[9] Boelens, O. J., Badcock, K. J., Görtz, S., Morton, S. A., Fritz, W., Karman, S. L., Jr, Michal, T., and Lamar, J. E., "Description of the F-16XL Geometry and Computational Grids Used in CAWAPI," *Journal of Aircraft*, Vol. 46, No. 2, 2009, pp. 369–376. doi:10.2514/1.34852

[10] Eliasson, P., "EDGE, a Navier-Stokes Solver for Unstructured Grids," Finite Volumes for Complex Applications III: Problems and Perspectives, Hermes Penton Science, London, 2002, pp. 527–534.

[11] Jameson, A., "Time-Dependent Calculations Using Multigrid, with Applications to Unsteady Flows Past Airfoils And Wings," AIAA Paper 91-1596, 1991.

[12] Wallin, S., and Johansson, A., "A Complete Explicit Algebraic Reynolds Stress Model for Incompressible and Compressible Turbulent Flows," *Journal of Fluid Mechanics*, Vol. 403, Jan. 2000, pp. 89–132. doi:10.1017/S0022112099007004

[13] Wilcox, D. C., "Reassessment of the Scale-Determining Equation for Advanced Turbulence Models," *AIAA Journal*, Vol. 26, No. 11, 1988, pp. 1299–1310. doi:10.2514/3.10041

[14] Hellsten, A. K., "New Advanced k-ω Turbulence Model for High-Lift Aerodynamics," *AIAA Journal*, Vol. 43, No. 9, 2005, pp. 1857–1869. doi:10.2514/1.13754

[15] Wallin, S., and Johansson, A. V., "Modelling Streamline Curvature Effects in Explicit Algebraic Reynolds Stress Turbulence Models," *International Journal of Heat and Fluid Flow*, Vol. 23, No. 5, 2002, pp. 721–730. doi:10.1016/S0142-727X(02)00168-6

[16] Hanjalic, K., Jakirlic, S., and Hadzic, I., "Computation of Oscillating Turbulent Flows at Transitional Re-Numbers," *Turbulent Shear Flows 9*, Springer–Verlag, Berlin, 1995, pp. 323–342.

[17] Peng, S.-H., "Hybrid RANS-LES Modeling Based on Zero- and One-Equation Models for Turbulent Flow Simulation," *Proceedings of the 4th International Symposium on Turbulence and Shear Flow Phenomena*, Vol. 3, 27–29 June 2005, pp. 1159–1164.

[18] Peng, S.-H., "Algebraic Hybrid RANS-LES Modelling Applied to Incompressible and Compressible Turbulent Flows," AIAA Paper 2006-3910, 2006.

[19] Spalart, P. R., Jou, W.-H., Strelets, M., and Allmaras, S. R., "Comments on the Feasibility of LES for Wings, and on a Hybrid RANS/LES Approach," *Advances in DNS/LES, 1st AFOSR International Conference on DNS/LES*, Greyden Press, Columbus, OH, Aug. 1997.

[20] Spalart, P. R., "Young-Person's Guide to Detached-Eddy Simulation Grids," NASA TR CR-2001-211032, 2001.

[21] Strang, W. Z., Tomaro, R. F., and Grismer, M. J., "The Defining Methods of Cobalt: A Parallel, Implicit, Unstructured Euler/Navier-Stokes Flow Solver," AIAA Paper 99-0786, Jan. 1999.

[22] Spalart, P. R., and Allmaras, S. R., "A One-Equation Turbulence Model for Aerodynamic Flows," AIAA Paper 92-0439, 1992.

[23] Tomaro, R. F., Strang, W. Z., and Sankar, L. N., "An Implicit Algorithm for Solving Time Dependent Flows on Unstructured Grids," AIAA Paper 1997-0333, 1997.

[24] Grismer, M. J., Strang, W. Z., Tomaro, R. F., and Witzeman, F. C., "Cobalt: A Parallel, Implicit, Unstructured Euler/Navier-Stokes Solver," *Advances in Engineering Software*, Vol. 29, Nos. 3–6, 1998, pp. 365–373. doi:10.1016/S0965-9978(97)00075-6

[25] Karypis, G., Schloegel, K., and Kumar, V., "Parmetis: Parallel Graph Partitioning and Sparse Matrix Ordering Library, Ver. 3.1," Technical Report, Department of Computer Science, University of Minnesota, Minneapolis, MN, 2003.

[26] Spalart, P. R., Deck, S., Shur, M. L., Squires, K. D., Strelets, M. K., and Travin, A., "A New Version of Detached-Eddy Simulation, Resistant to Ambiguous Grid Densities," *Theoretical & Computational Fluid Dynamics*, Vol. 20, 2006, pp. 181–195. doi:10.1007/s00162-006-0015-0

[27] Frink, N. T., Pirzadeh, S. Z., Parikh, P. C., Pandya, M. J., and Bhat, M. K., "The NASA Tetrahedral Unstructured Software System," *The Aeronautical Journal*, Vol. 104, No. 1040, Oct. 2000, pp. 491–499.

[28] Mavripilis, D. J., "Unstructured Mesh Discretizations and Solvers for Computational Aerodynamics," AIAA Paper 2007-3955, 2007.

[29] Mavripilis, D. J., "Solution of the Two-Dimensional Euler Equations on Unstructured Triangular Meshes," Ph.D. Thesis, MAE Department, Princeton University, Princeton, NJ, 1987.

[30] Cummings, R. M., Morton, S. A., and Siegel, S. G., "Computational Simulation and Experimental Measurements for a Delta Wing with Periodic Suction and Blowing," *Journal of Aircraft*, Vol. 40, No. 5, 2003, pp. 923–931. doi:10.2514/2.6868

[31] Vassberg, J. C., Tinoco, E. N., Mani, M., Brodersen, O. P., Eisfeld, B., Wahls, R. A., Morrison, J. H., Zickuhr, T., Laflin, K. R., and Mavriplis, D. J., "Summary of the Third AIAA CFD Drag Prediction Workshop," AIAA Paper 2007-0260, 2007.

[32] Lamar, J. E., "Cranked Arrow Wing (F-16XL-1) Flight Flow Physics with CFD Predictions at Subsonic and Transonic Speeds," *RTO Applied Vehicle Technology Panel (AVT) Symposium*, NATO Research and Technology Office, Paris, France, 7–10 May 2001, pp. 44-1–44-20; also RTO, MP-69-P-44.

[33] Degani, D., and Schiff, L., "Computation of Supersonic Viscous Flows Around Pointed Bodies at Large Incidence," AIAA Paper 1983-0034, 1983.

[34] Menter, F. R., Kuntz, M., and Langtry, R., "Ten Years of Industrial Experience with the SST Turbulence Model," *Turbulence, Heat and Mass Transfer*, Vol. 4, edited by K. Hanjalic, Y. Nagano, and M. Tummers, Begell House Inc., Reading, CT, 2003, pp. 625–632.

[35] Menter, F. R., Kuntz, M., "Adaptation of Eddy-Viscosity Turbulence Models to Unsteady Separated Flow Behind Vehicles," *Symposium on "The Aerodynamics of Heavy Vehicles: Trucks, Buses and Trains,"* edited by R. McCallen, F. Browand, and J. Ross, Springer, Berlin, 2–6 Dec. 2002, 2004.

[36] Cummings, R. M., Morton, S. A., Siegel, S. G., and Bosscher, S., "Numerical Prediction and Wind Tunnel Experiment for a Pitching Unmanned Combat Air Vehicle," AIAA Paper 2003-0417, 2003.